

**Performance Evaluation and Correction for Scatter and
Attenuation on the LabPET4™ Positron Emission
Tomography System**

by

Tyler Dumouchel, B.Sc.

A Thesis Submitted to
the Faculty of Graduate Studies and Research
in Partial Fulfillment of
the Requirements for the Degree of
Master of Science

Ottawa-Carleton Institute for Physics
Department of Physics, Carleton University
Ottawa, Ontario, Canada
Submitted July, 2007

©copyright
2007, Tyler Dumouchel



Library and
Archives Canada

Bibliothèque et
Archives Canada

Published Heritage
Branch

Direction du
Patrimoine de l'édition

395 Wellington Street
Ottawa ON K1A 0N4
Canada

395, rue Wellington
Ottawa ON K1A 0N4
Canada

Your file *Votre référence*
ISBN: 978-0-494-33698-4
Our file *Notre référence*
ISBN: 978-0-494-33698-4

NOTICE:

The author has granted a non-exclusive license allowing Library and Archives Canada to reproduce, publish, archive, preserve, conserve, communicate to the public by telecommunication or on the Internet, loan, distribute and sell theses worldwide, for commercial or non-commercial purposes, in microform, paper, electronic and/or any other formats.

The author retains copyright ownership and moral rights in this thesis. Neither the thesis nor substantial extracts from it may be printed or otherwise reproduced without the author's permission.

AVIS:

L'auteur a accordé une licence non exclusive permettant à la Bibliothèque et Archives Canada de reproduire, publier, archiver, sauvegarder, conserver, transmettre au public par télécommunication ou par l'Internet, prêter, distribuer et vendre des thèses partout dans le monde, à des fins commerciales ou autres, sur support microforme, papier, électronique et/ou autres formats.

L'auteur conserve la propriété du droit d'auteur et des droits moraux qui protègent cette thèse. Ni la thèse ni des extraits substantiels de celle-ci ne doivent être imprimés ou autrement reproduits sans son autorisation.

In compliance with the Canadian Privacy Act some supporting forms may have been removed from this thesis.

Conformément à la loi canadienne sur la protection de la vie privée, quelques formulaires secondaires ont été enlevés de cette thèse.

While these forms may be included in the document page count, their removal does not represent any loss of content from the thesis.

Bien que ces formulaires aient inclus dans la pagination, il n'y aura aucun contenu manquant.


Canada

Abstract

The LabPET4™ camera is the world's first commercial avalanche photodiode (APD) PET system. The new technology is expected to yield high resolution and count rates for small animal imaging due to quasi-individual crystal-APD coupling and highly parallel digital electronics. An automated quality assurance test was developed to verify that the scanner was operating correctly on a daily basis. Initial performance evaluation measurements including sensitivity, noise equivalent count rate, scatter fraction, dead time, image resolution and uniformity were performed to determine the scanner's capability for cardiac imaging in rats and mice. Finally, the magnitude of attenuation and scatter was studied in phantoms on the order of rat and mouse sizes, and algorithms were explored to correct for these phenomena. The performance measures suggest that the system is capable of tracer uptake imaging in small animals and that attenuation and scatter correction are necessary to obtain accurate images of the tracer distribution.

Statement of Originality

Some of the work discussed in this thesis was presented at two conferences. Some of my work was published in the conference proceedings of the 2006 Nuclear Science Symposium and Medical Imaging Conference [1] and as an abstract at the 2007 Society of Nuclear Medicine Annual Meeting [2]. I contributed to the work published in [1] by designing and performing the experiments, creating the method for the analysis and performing the analysis, and writing the first draft of the paper. The coauthors took part in reviewing the draft. For my second contribution [2] I performed the experiments and analyzed the data that are presented in my thesis. The first draft of the presentation was created by me. The coauthors analyzed one of the experiments that appear in the presentation; however, this work does not appear in my thesis. They also helped edit the presentation.

Acknowledgements

I would first like to thank my supervisor, Rob deKemp, for his exceptional guidance throughout the duration of my research here at the University of Ottawa Heart Institute. I am especially grateful for the time and effort he invested to ensure that the goals of my project were fulfilled.

I am also indebted to the employees and students in the cardiac PET unit and the radiochemistry laboratory at the University of Ottawa Heart Institute because without their help and support this project would have not been possible. They have truly made my experience here an enjoyable one.

Finally, I would like to thank Advanced Molecular Imaging for their technical support and many interesting discussions.

Table of Contents

List of Tables	vi
List of Figures	vii
Glossary of Acronyms	ix
Introduction	x
Chapter 1 - Theory	1
1.1 Positron Emission	1
1.2 Positron Range and Annihilation	1
1.3 Gamma Ray Interactions.....	3
1.4 Coincidence Detection	5
1.5 Data Correction	8
1.6 Image Reconstruction	10
Chapter 2 – LabPET4™ System Information	18
2.1. Introduction to the LabPET4™ Scanner.....	18
2.2. Avalanche Photodiodes.....	18
2.3. LabPET4™ Specifications.....	19
2.4. Data Acquisition, Handling and Reconstruction.....	21
2.5. Available Corrections on the LabPET4™ System.....	24
Chapter 3 – Quality Assurance	26
Chapter 4 – Performance Evaluation of the LabPET4™ Camera	33
4.1. Motivation.....	33
4.2. System Absolute Sensitivity	34
4.3. Noise Equivalent Count Rate and Scatter Fraction.....	36
4.4. System Dead Time	48
4.5. Reconstructed Image Resolution	50
4.6. Image Non-Uniformity	60
4.7. Assessment of Attenuation and Scatter.....	62
4.8. System Comparison	65
Chapter 5 –Attenuation and Scatter Correction	71
5.1. Introduction.....	71
5.2. Attenuation Correction.....	72
5.3. Scatter Correction	76
5.4. Discussion	88
Chapter 6 - Conclusion	97
Appendix A – Cardiac Rat Phantom.....	99
References	104

List of Tables

Table 1.1. Isotopes commonly used in PET.....	2
Table 1.2. Linear attenuation coefficients for various materials at 511 keV	4
Table 4.1. Expected system specifications for the LabPET4™	33
Table 4.2. Percentage dead time for the mouse-like and rat-like phantoms	50
Table 4.3. Reconstructions performed to assess the resolution	52
Table 4.4. Simulated peak recovery ratios for holes of different sizes.....	54
Table 4.5. Comparison of the performance parameters of the LabPET4™	69
Table 5.1. Comparison of the ratios for the cold and hot ROIs	84

List of Figures

Figure 1.1. Illustration of the different types of coincidences in PET imaging.....	7
Figure 1.2. The forward projection	11
Figure 1.3. Illustration of the contribution of direct and oblique LORs	12
Figure 2.1. Illustration of the alternating rings of different scintillator crystal types	20
Figure 2.2. The offset detector spacing on the LabPET4™ scanner	22
Figure 3.1. Reconstructed transmission images.....	29
Figure 3.2. Plot of statistics for the QA transmission images.....	30
Figure 4.1. Rat phantom design	38
Figure 4.2. A summed profile of the aligned prompt data.....	40
Figure 4.3. Plot of the different count rates for the mouse-like phantom	43
Figure 4.4. Plot of the different count rates for the rat-like phantom	43
Figure 4.5. An expanded view of the NEC curve for the mouse-like phantom.....	44
Figure 4.6. An expanded view of the NEC curve for the rat-like phantom	44
Figure 4.7. Comparison between the measured true rate (blue) and the ideal true rate (red).....	49
Figure 4.8. Comparison between the measured true rate (blue) and the ideal true rate (red).....	49
Figure 4.9. The Micro Deluxe Phantom™ with a hot rods insert.....	51
Figure 4.10. Reconstructed image of the Micro Deluxe Phantom™.....	52
Figure 4.11. The images used for convolution.....	54
Figure 4.12. Reconstructed image resolution of MLEM	56
Figure 4.13. Transverse images of the rat phantom with lines drawn across	58
Figure 4.14. Cardiac images of the LV in a mouse and rat.....	59
Figure 4.15. Central transverse image of the uniform flood phantom.....	61
Figure 4.16. Plot of the maximum, mean and minimum values	61
Figure 4.17. Profile across the uniformity phantom	63
Figure 5.1. Central transverse images of (a) non-corrected and (b) attenuation corrected data.....	76
Figure 5.2. Illustration of the cold rod phantom used for scatter correction.....	80
Figure 5.3. Profiles for a row in the sinogram to show the effect of scatter correction...	82
Figure 5.4. Regions of interest (ROI) drawn on the scatter correction phantom.....	83

Figure 5.5. The cold rod phantom (a) before and (b) after scatter correction.....	85
Figure 5.6. Chord length calculation through a circular object	86
Figure 5.7. Calculated attenuation correction	87
Figure 5.8. Profiles across the ACF sinograms.....	90
Figure A.1. Exposed thoracic cavity of a 285 g rat.....	100
Figure A.2. The cardiac rat phantom	103

Glossary of Acronyms

ACF – attenuation correction factor
APD – avalanche photodiode
AR – activity region
DICOM – digital imaging and communications in medicine
DS – double sampling
ECG – electrocardiogram
FBP – filtered back projection
FORE – Fourier rebinning
FOV – field of view
FWHM – full width at half maximum
HLA – horizontal long axis
LGSO - Lutetium Gadolinium oxyorthosilicate
LOR – line of response
LSO – Lutetium oxyorthosilicate
LV – left ventricle
LYSO – Lutetium Yttrium oxyorthosilicate
MAU – mean activity uptake per pixel
MIP – maximum intensity projection
MLEM – maximum likelihood expectation maximization
MSB – mean scatter background per pixel
MWPC – multiwire proportional chamber
NEC – noise equivalent count
OPLEM - one pass list mode expectation maximization
OSEM – ordered subset expectation maximization
PET – positron emission tomography
PMT – photomultiplier tube
QA – quality assurance
ROI – region of interest
RS – regular sampling
SA – short axis
SB – scatter background
SNR – signal to noise ratio
SSRB – single slice rebinning
VLA – vertical long axis

Introduction

Positron Emission Tomography (PET) is a powerful non-invasive 3D imaging modality that has the ability to provide detailed information about various physiological processes. A molecule that follows a specific process inside the body is labelled with a positron emitting isotope and is then administered into the subject. The molecule is termed a tracer and the reconstructed images represent the tracer distribution inside a subject, which is related to the biochemical function. PET has found a variety of applications, namely in heart disease, cancer diagnostics, and drug development. This modality has been used to perform clinical research on humans; however, with growing interest in genomics research, new alternatives are being introduced for imaging in small animals, especially in mice which have 99% of their mammalian genome in common with humans [3].

The University of Ottawa Heart Institute purchased their first PET camera for human cardiac imaging in 1995. In 2002 a cyclotron and radiochemistry laboratory, both necessary for tracer production, were constructed on site creating a complete unit devoted to clinical research and diagnostics. In April 2006 an Avalanche Photodiode (APD) based small animal PET camera, LabPET4™, was purchased by the Heart Institute from Advanced Molecular Imaging (Sherbrooke, QC), intended to introduce a new realm of research at the Heart Institute. The goal of the camera is to provide a means for molecular imaging in small animals, particularly rats and mice, to study the manifestation of genetic defects in these animals. Once a gene has been identified in humans to have an influence on disease it can be translated into an animal model. This translation can be

achieved by the introduction of the gene into the animal or through removal of an analogous gene. The camera is therefore used to probe into the animal-adapted models of human disease. It provides a means to investigate the mechanisms of human disease, and to develop as well as test new treatments. Furthermore, the on-site cyclotron allows novel tracers to be developed which can be tested on the small animal system as a precursor to clinical trials. The studies may then be translated back into humans with the objective to better understand heart function and disease. The major advantage of PET is that it is non-invasive allowing for an animal to serve as its own control and it permits for longitudinal studies in the same animal. The use of animals not only accelerates research but it offers the ability to control the environment.

It is vital that the images obtained with PET are representative of the tracer distribution inside a subject. Phenomena such as detector efficiency variations, detector dead time, random coincidences, photon attenuation and photon scatter deteriorate image quality by producing image artifacts and limiting the quantitative accuracy of the system. These phenomena must be examined in detail to understand their order of magnitude and to ensure correction techniques provide a means to properly address these problems. The LabPET4™ system has recently been introduced to the commercial market and with the advent of a new system comes performance testing to ensure that the system is capable of performing a given imaging task and to assess the accuracy of the images produced. Finally, the accuracy of the available corrections for detector efficiency and random coincidences must be verified and other correction techniques for scatter and attenuation must be explored.

Project Overview

The basic underlying principles of PET, including data acquisition and reconstruction, are reviewed in Chapter 1. The LabPET4™ system information and a discussion on the technology it offers are discussed in Chapter 2. Chapter 3 addresses quality assurance testing and provides a methodology for performing this task on a daily basis. The performance testing and imaging capability are examined in Chapter 4. This section demonstrates the evaluation of the scanner's performance for cardiac imaging in small animals and assesses which corrections are required to obtain quantitative images of the tracer distribution. The work presented in section 4.5 on MLEM reconstructed image resolution was published in the conference proceedings of the 2006 Nuclear Science Symposium and Medical Imaging Conference [1]. The results from sections 4.2, 4.3, 4.5 and 4.6 were presented as an abstract for the 2007 Society of Nuclear Medicine Annual Meeting [2]. The final chapter addresses attenuation and scatter correction and provides a review outlining established methods used for obtaining these corrections. It also discusses preliminary evaluation on scatter and attenuation correction in phantoms in order to understand if these corrections will improve image quality and to determine if they are necessary in small animals.

Chapter 1 - Theory

1.1 Positron Emission

Nuclei with an excess of either protons or neutrons are subject to radioactive decay resulting in a more stable nucleus. Positron emission, or beta plus decay, is a phenomenon that may occur when a nucleus has an excess number of protons. In this case, a proton in the nucleus will be converted into a neutron releasing a positron and an electron neutrino. The decay process for positron emission is illustrated below:



where X/Y are the parent/daughter isotopes, respectively.

A competing decay process for proton rich nuclei is electron capture where the nucleus may capture an orbiting electron, which converts a proton into a neutron. Positron emission is only possible if the parent-daughter rest mass energies exceed an energy difference of $2m_e c^2$ where m_e is the mass of an electron. A factor of two is appropriate because the nucleus releases a positron and the atom loses an additional electron to preserve charge. If this condition is not satisfied the nucleus will decay exclusively by electron capture.

1.2 Positron Range and Annihilation

The remaining energy from the above reaction is carried away as kinetic energy shared between the neutrino and positron. The positron will thus have a continuous energy spectrum ranging from zero up to a maximum energy described by:

$$E_{\max} = (m_x - m_y - 2m_e)c^2 \quad (1.2)$$

where m_x/m_y are the mass of the parent/daughter isotopes.

Once the positron is emitted it will lose energy rapidly due to inelastic interactions with electrons in the surrounding media. After the positron loses sufficient energy and reaches thermal levels (~ 10 eV) it will typically annihilate with an electron producing two 511 keV photons in opposite directions in order to conserve energy and momentum. Another phenomenon may also occur where the positron annihilates in flight resulting in photons that are not emitted at 180° from each other. Table 1.1 displays the maximum and mean energies and ranges for positrons emitted from some commonly used PET isotopes.

Table 1.1. Isotopes commonly used in PET [4].

Isotope	Half Life (min)	Max Energy (MeV)	Mean Energy (MeV)	Max Range (mm)	Mean Range (mm)
^{18}F	110	0.635	0.250	2.3	0.35
^{11}C	20.3	0.96	0.386	4.1	0.56
^{13}N	10.0	1.19	0.492	5.2	0.72
^{15}O	2.1	1.72	0.735	8.1	1.1
^{82}Rb	1.3	3.35	1.52	16.7	2.4

The F, C, N, and O isotopes are typically produced using a cyclotron through proton bombardment on a target material while ^{82}Rb is produced by a generator from ^{82}Sr decay. These various isotopes may be incorporated into molecules known as radiolabeled tracers. The tracers are injected into subjects and may either mimic a physiological process (analog) or directly follow a physiological process. Examples of this are ^{18}F -fluorodeoxyglucose (FDG), which is a glucose analog because it is taken up by the cell but not metabolized, or ^{11}C -glucose, which follows the complete glycolytic pathway inside the cell. Once inside a subject, the molecule will travel through the body and the emitted positrons will encounter electrons. After annihilation occurs two 511 keV photons are released and travel approximately 180° away from each other. Because the

electron and positron may have momentum when they annihilate, the emitted angles will have an approximate Gaussian distribution around a mean of 180° with a FWHM = 0.5° [5], which is known as non-collinearity. The simultaneous detection of this radiation is what forms the basis of PET imaging.

1.3 Gamma Ray Interactions

The 511 keV gamma rays emitted in the annihilation process must travel through matter prior to being detected. Photons traversing matter may undergo various interactions in the media including coherent scattering, photoelectric absorption, Compton scattering and pair production. In PET the annihilation photons do not have sufficient energy to induce pair production as the energy must exceed 1.022 MeV for this process to occur. Furthermore, the coherent scattering cross section is negligible at 511 keV in comparison to the other gamma ray interactions. The predominant processes are thus photoelectric absorption and Compton scattering. Photoelectric absorption occurs when an incoming photon interacts with an atom in the media by transferring all of the photon energy to an orbital electron. As a result, an electron is released and is then quickly absorbed in the surrounding media. The probability for a photoelectric interaction per unit distance is described by $\mu_{pe}(\text{cm}^{-1})$. The probability for this interaction to occur per atom is roughly proportional to Z^{3-4} at 511 keV [5]. In Compton scattering the incoming photon interacts with a loosely bound or free electron and in order to conserve energy and momentum the photon scatters at an angle θ with energy $h\nu'$ given by the relationship:

$$h\nu' = \frac{h\nu}{1 + \frac{h\nu}{m_e c^2} (1 - \cos(\theta))} \quad (1.4)$$

The remaining energy is transferred to the recoil electron. The probability per unit distance for this type of interaction to occur is described by $\mu_C(\text{cm}^{-1})$ and because this process depends on the number of electrons, the probability of interaction per atom increases linearly with Z [6].

The overall probability for a photon at 511 keV to interact in a medium per unit distance is described by the linear attenuation coefficient μ where:

$$\mu = \mu_C + \mu_{pe}. \quad (1.5)$$

For a monoenergetic and narrow beam geometry, the intensity of the beam that penetrates the medium can be written as:

$$I = I_o e^{-\int \mu(x) dx} \quad (1.6)$$

where I_o is the initial beam intensity and I is the beam intensity after passing through a distance x of the medium. Table 1.2 gives various interaction coefficients for some materials.

Table 1.2. Linear attenuation coefficients for various materials at 511 keV [5].

Material	$\mu_C (\text{cm}^{-1})$	$\mu_{pe} (\text{cm}^{-1})$	$\mu (\text{cm}^{-1})$
Soft Tissue/Water	0.096	0.00002	0.096
Bone	0.169	0.001	0.17
Bismuth Germanate	0.54	0.40	0.96
Lead	0.76	0.89	1.78
Tungsten	1.31	1.09	2.59
Lutetium oxyorthosilicate (LSO)	0.58	0.30	0.88

The case discussed assumes narrow beam geometry, however, in PET we generally consider broad beam geometry. This is the case since collimation is not typically used in current PET systems. Furthermore, the dominant photon interaction in soft tissue is Compton scattering. Acceptance of the scattered photons will cause the

apparent attenuation coefficient to decrease because some of the scattered photons will still be detected. This phenomenon is referred to as photon buildup.

1.4 Coincidence Detection

PET works on the principle that both of the annihilation photons originating from a single decay event within a subject are detected simultaneously; this is referred to as coincidence detection. Typically these measurements are obtained using a scintillator crystal that is coupled to a photodetector, such as a photomultiplier tube (PMT), or a solid state photodetector, such as an avalanche photodiode (APD). There are also other detection methods that have been explored for PET including multiwire proportional chambers (MWPC) and direct detection using semiconductors (eg. CZT). MWPCs are devices that generate electrical signals down wire arrangements when an electron comes into contact with the anode wire. They allow for high spatial resolution necessary for PET. Photons strike an input lead converter, which converts the photons to photoelectrons which can then be detected. For direct detection, photons directly create electron/hole pairs in the semiconductor material, which produces an output current that can be measured. Detectors are usually arranged in a circular ring geometry that defines a transaxial plane. Multiple rings are then stacked axially to compose a complete scanner with 3D volume coverage.

Each detector measures single events and information, such as the time and energy of an event, is recorded. A coincidence timing window and energy window are then applied to the singles data to organize the events in coincidences and to discriminate against unwanted events. In deciding the width of a coincidence window one must take into consideration the timing resolution of each detector channel in coincidence along

with the time it takes a photon to travel to a detector. The coincidence timing window is typically given by 2τ where τ is defined as the FWHM of the spectrum of coincidence timing pulses. A coincidence event that falls within the given timing window is referred to as a prompt coincidence. The energy window has a lower threshold as well as an upper threshold. The lower threshold helps remove events which have undergone Compton scatter, while the upper threshold discriminates against multiple interactions within a detector. The choice for this window is dependent upon the distribution of energies that a detector will record. The singles rates are much higher than coincidence rates because of different geometric apertures.

Once a coincidence event has been established, the event can be recorded into what is known as list mode format. Here the time of arrival of the event along with the energy and positional information are stored on an event-by-event basis. Each event is identified as a line of response (LOR), which joins the two coincident detectors together in space. A recorded coincidence is therefore indicative than an annihilation event occurred on the LOR joining two detectors as the photons are emitted at $\sim 180^\circ$ apart from each other. Coincidence detection is also termed electronic collimation because it uses the collected information to position an event so that physical detector collimators are not needed. A large number of coincidence events are then recorded when scanning a subject. These events are sampled from many LORs over the volume of the field of view (FOV), thereby covering a range of sampling angles and radial offsets.

There are three main types of prompt coincidences that may be recorded inside a PET scanner including true coincidences, random coincidences and scattered coincidences. These are illustrated in Figure 1.1. A true coincidence is recorded when

neither annihilation photon undergoes any interactions and is directly detected within the designated timing window, as shown in Figure 1.1(a). Random coincidences occur when two uncorrelated single events are recorded in coincidence by chance. This occurs when two annihilation events take place at the same time and only one photon from each event is recorded due to attenuation of the corresponding photons in the medium or because the photons have left the imaging plane. This results in the counting of an event that is registered incorrectly. This randoms rate can be described by the equation:

$$R = \tau_c S_1 S_2 \quad (1.7)$$

where R is the randoms rate, τ_c is the width of the coincidence timing window and S_1 and S_2 are the singles rates at each detector. As can be perceived by the equation, the randoms rate will increase as the square of the activity in the FOV because the singles rates are directly proportional to the activity in the FOV. Lastly, a scattered coincidence occurs when one or both of the annihilation photons undergo a Compton scatter event.

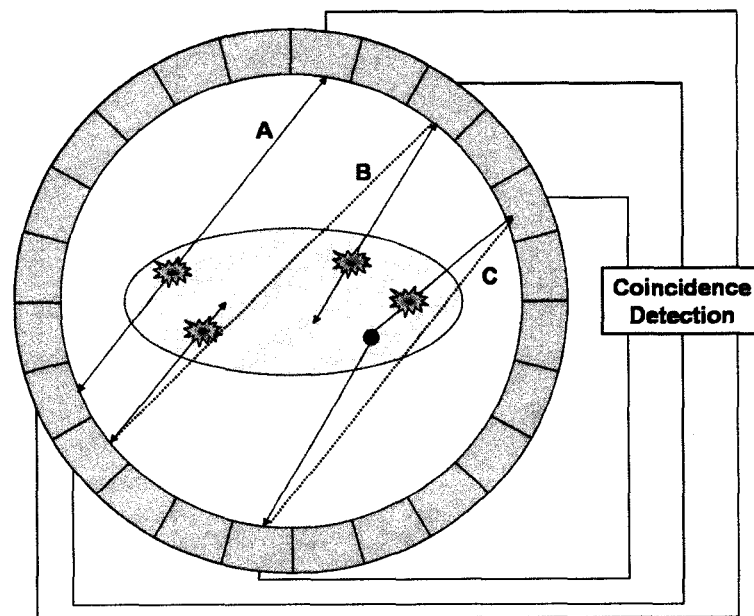


Figure 1.1. Illustration of the different types of coincidences in PET imaging: (a) true coincidence, (b) random coincidence and (c) scattered coincidence.

Considering equation 1.4, we see that when a photon deflects at an angle θ off of an electron, the energy of the photon is reduced and the direction is changed. Depending on the chosen energy window, a number of these events may still be recorded. Again, the result is an event that will be registered incorrectly, as can be identified in Figure 1.1(C). Both the randoms and scattered coincidences are regarded as undesirable events and in general measures are taken to reduce these effects.

1.5 Data Correction

The positron emission data obtained has inherent limitations due to the detection system and gamma ray interactions. The detection system limitations are in the form of detection efficiency, detection dead time, and random events. Compton scatter also poses a problem in PET because it will contribute to mispositioned events and attenuation in the recorded data. These limitations will tend to reduce the accuracy of the data and must therefore be addressed.

Non-uniformities may arise in the reconstructed images as a result of individual detector responses and the sampling geometry of the scanner. The response will differ between each detector due to physical variations in the crystal and electronics' fabrication processes. Furthermore, detectors are not perfectly arranged in a circular geometry resulting in variable physical spaces between detectors, which leads to geometric non-uniformities. The correction for these phenomena is referred to as normalization. Normalization is obtained through multiplication of the total counts in each individual LOR by a measured correction factor, or a product of individual detector efficiencies and calculated geometric efficiencies [5]. The correction factors can be acquired by placing a source of uniform activity in the FOV. Some common sources are a uniform cylindrical

phantom that is placed at the center of the scanner, or a rotating rod source that uniformly rotates close to the detector faces outside of the imaging FOV; a rotating source may also be utilized for attenuation correction. In both cases, the sources could be constructed from a long-lived positron emitting isotope such as ^{68}Ge . This is an ideal source because of its long half life of 271 days, which enables it to be used on a daily basis.

Additionally, the source used has a low activity so that randoms do not saturate the scanner and dead time effects are small. Data are acquired using the source, then the correction factors are derived from the inverse of the recorded counts.

Dead time is an effect that will tend to produce non-linearities in the prompt count rate and is most apparent when acquiring with a high activity in the FOV. This phenomenon arises when a photon strikes a detector while an event is already being processed by the system. The count rate should ideally increase linearly with activity; however, due to this effect the count rate will begin to drop below the linear expectation at higher activities. At even higher activities the count rate may begin to decrease.

There are two general models used to correct for dead time. The first is referred to as paralyzable and the second is non-paralyzable. In a paralyzable system the dead time is extended when another photon strikes a detector while the system is processing an event. In the non-paralyzable system, a second photon striking the detector during processing will be ignored. Dead time correction is typically done by applying one of the two models or a combination of both [5].

During data acquisition the measurement of random coincidences is inevitable with a finite coincidence timing window, especially when high activity is present as is noted from equation 1.7. These events must therefore be subtracted from the total prompt

events to obtain the true event rate. Randoms may be corrected by applying equation 1.7 to the singles event rates between two detectors and then subtracting these events along the LOR connecting the detectors. An alternative approach is performing randoms correction using a delayed window technique. In the delayed coincidence window technique a single event at one detector is recorded within a defined timing window (eg. 2τ). This event is then related to other independent single events falling in a time $\Delta t \pm \tau$ where Δt is large enough (eg. 100 ns) so that the two events are uncorrelated because they can not originate from the same decay. This is done for all possible LORs inside the scanner. The random coincidences are then subtracted from the prompts to obtain the true and scattered coincidences.

Photon attenuation occurs when photons pass through an object and this phenomenon is approximately governed by equation 1.6. Attenuation results in the loss of events or the reappearance of a photon at a lower energy and a different angle due to Compton scatter. Correction for this phenomenon has been explored in much detail [7-12] and methods for obtaining this correction will be discussed in Chapter 5. Finally, photon scatter originating from within the object, gantry and detectors will produce a spatial blurring of counts throughout an image. Again various methods for obtaining correction for this phenomenon has been explored in much detail [13-23] and will be addressed in Chapter 5.

1.6 Image Reconstruction

The data obtained with PET can be organized in projection format, meaning they are the collection of line integrals along multiple LORs through an object. The list mode data are generally rebinned into what are known as sinograms where each element

corresponds to a specific LOR as defined by a radial and angular address. The value in each element thus represents the line integral of activity along a particular LOR defined by r and θ through the object, which is approximately the total number of annihilation pairs detected at that point. The term sinogram is adopted because a point in image space will trace out a sine wave in projection space. The forward projection process is shown in Figure 1.2 for two uniform circles of activity. The collection of line integrals along one angle by varying the radial component is referred to as a parallel projection. On most current commercial scanners data are acquired in 3D, meaning that all possible LORs within the scanner are included and they are not restricted by detector collimators to independent transaxial planes.

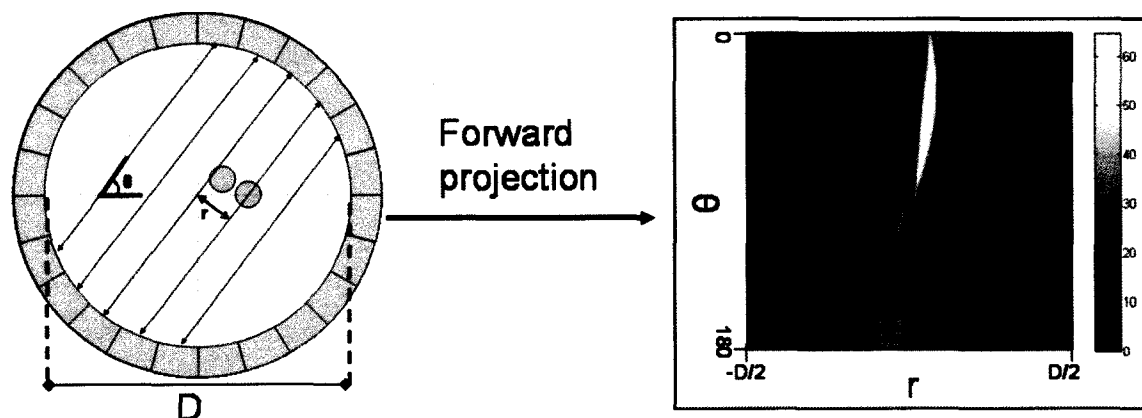


Figure 1.2. The forward projection of two circular objects in image space to sinogram format. Each bin in the sinogram is the line integral through the object along an LOR given by r and θ . The diameter of the ring is given by D .

The projection data obtained using the PET methodology thus represent the distribution of activity within a subject. The goal in PET, is to accurately reconstruct the spatial distribution of positron decays in a subject using these projection data quantitatively (ie. Bq/mL). Two common methods are generally used to reconstruct data including filtered backprojection (FBP) and iterative techniques such as maximum

likelihood expectation maximization and ordered subset expectation maximization.

While most commercial scanners operate in 3D acquisition mode, data are often rebinned or transformed into an equivalent 2D data set so that 2D reconstruction programs may still be used. The following discussion will be restricted to the 2D case as 3D reconstruction is not utilized in this work. In order to obtain 2D projections from 3D data, the oblique LORs, those not from 2D transaxial planes, must be repositioned into a direct or cross plane. A direct plane is defined by a transaxial ring of detectors while a cross plane is formed by creating a fictitious plane between two adjacent direct planes. This concept is illustrated in Figure 1.3.

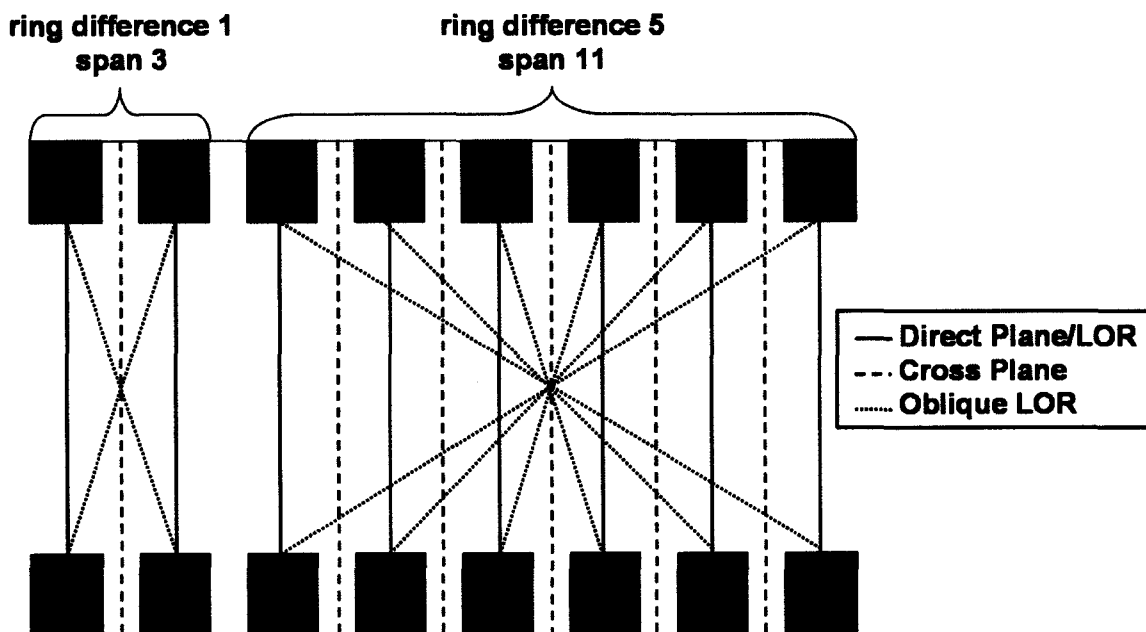


Figure 1.3. Illustration of the contribution of direct and oblique LORs to a direct and cross plane. The concept of span and ring difference is also illustrated to demonstrate the overall contribution of LORs for a given ring difference and span. The black boxes represent the detectors.

There are two common methods for rebinning the 3D data set into its 2D equivalent. These are known as single slice rebinning (SSRB) and Fourier rebinning (FORE). In SSRB the data are rebinned through positioning of the 3D data into the

corresponding 2D location by taking the average of the axial location of an event, then placing the event in that related axial position in the 2D direct or cross plane sinograms. The principle governing FORE is relating the Fourier transform of oblique sinograms to the Fourier transform of transverse (direct or cross plane) sinograms. FORE generates superior results in comparison to SSRB [5] because of improved spatial localization in projection space leading to enhanced resolution, however, it is more computationally intensive [24] because it involves Fourier analysis rather than spatial averaging. After rebinning is concluded, the data are then available for 2D reconstruction.

Two important concepts for data rebinning are ring difference and span. The ring difference is classified by how many detectors are used axially to define the oblique LORs. If we used 6 detectors we would have a maximum ring difference of 5. Span is used to describe how much of the data are included during the rebinning process. For data to be rebinned with SSRB, the span is given by $2N+1$ where N is the ring difference. Thus if we have a total of 16 direct planes, the maximum ring difference one could obtain is 15 leading to a span of 31 for SSRB. Another way to envision the span is to count the total number of planes available with any given ring difference. From Figure 1.3 it is noticed for a ring difference of 5 the total number of direct and cross planes is 11 because data will span a total of 11 direct and cross planes. For the remainder of this work a span of 31 will refer to SSRB with a ring difference of 15.

Once the data have been rebinned, 2D reconstruction may commence. The reconstruction algorithm that enabled PET to become practical was FBP. FBP can be thought of as direct sinogram reconstruction and it works by uniformly redistributing filtered parallel projections along predefined lines in image space. FBP can be

demonstrated analytically by considering projection data represented by $g(r, \theta)$, where g is the line integral through an object along an LOR defined spatially by r and θ . This can be expressed as [25]:

$$g(r, \theta) = \int_{-\infty}^{\infty} \int_{-\infty}^{\infty} f(x, y) \delta(x \cos \theta + y \sin \theta - r) dx dy \quad (1.8)$$

where $f(x, y)$ is the activity distribution at a point (x, y) in image space and δ is the delta function. Equation 1.8 is known as the radon transform of $f(x, y)$. If the 1D Fourier transform of $g(r, \theta)$ is computed, the following relation can be established [25]:

$$G(\rho, \theta) = \int_{-\infty}^{\infty} g(r, \theta) e^{-i2\pi\rho r} dr = \int_{-\infty}^{\infty} \int_{-\infty}^{\infty} f(x, y) e^{-i2\pi\rho(x \cos \theta + y \sin \theta)} dx dy = F(u, v) \quad (1.9)$$

The integral thus takes the form of a 2D Fourier transform where (u, v) are the spatial frequencies corresponding to (x, y) , and ρ is the length of the line from the origin to the point (u, v) . If the inverse 2D Fourier transform is then computed the result is [25]:

$$f(x, y) = \int_0^{\pi} \int_{-\infty}^{\infty} |\rho| G(\rho, \theta) e^{i2\pi\rho(x \cos \theta + y \sin \theta)} d\rho d\theta \quad (1.10)$$

which is the analytical form of FBP that gives the activity distribution $f(x, y)$ given a collection of projections g . Equation 1.10 can be considered as the inverse Radon transform. To implement this on PET scanners, the analytical expression is discretized. Furthermore, the factor $|\rho|$ is referred to as the ramp filter and is an inherent property of FBP. Its effect is to produce a uniform frequency response through suppression of the lower frequencies and enhancement of the higher frequencies. Because of finite sampling, $|\rho|$ can be multiplied by an additional ‘windowing’ function. Noise generally occurs at higher frequencies, thus the window function may decrease higher frequencies so that noise is suppressed and does not translate into the final image.

Although they are more computationally intensive, iterative reconstruction techniques are generally preferred over FBP [5] because they do not require complete sampling to produce an image (ie. a dead detector channel will result in a streak artifact with FBP) and models of system geometry and counting statistics may be introduced into the reconstruction algorithm to provide improved accuracy in the final image. In essence, iterative reconstruction methods proceed in the following manner: an initial image estimate is made; usually blank or uniform. A forward projection is then computed and compared to the measured projection data by taking a difference for example. Adjustments are then made to the estimated image, then the process continues until the estimated and measured projection are comparable.

The most popular iterative technique is known as maximum likelihood expectation maximization (MLEM). Likelihood is a statistical quantity that is maximized when the difference between the measured and estimated projection data are minimized. The expectation maximization algorithm is an iterative algorithm that maximizes this likelihood under a Poisson data model [5]. The algorithm treats the measured projection data as having a Poisson distribution which is determined by the counting statistics in each LOR. A system model is derived from the geometry and detection response function of the scanner. The model provides the probability of a gamma ray being detected within a specific LOR. It is derived from simulations of point sources placed inside the scanner [5]. The algorithm then uses this system model to iteratively find a match between the measured projection and estimated projections.

A more efficient approach to MLEM has been introduced to increase the speed of convergence. This is known as ordered subset expectation maximization (OSEM). This

algorithm proceeds in a similar fashion to MLEM, but in this case only a subset of the angular data is utilized for each iteration. An example would be to use every second angle for the first iteration, then on a second iteration, one would utilize the complementary part of the data and this would continue to alternate. This results in an iterative reconstruction approach that has accelerated convergence, where the time for an iteration is proportional to the number of angles used.

Iterative reconstruction methods have several advantages in comparison to FBP. First the system model used accurately reflects the detection probability of a gamma ray originating from a specific location in an object. This can offer an improved spatial resolution because of exact spatial positioning of the emitted gamma ray. Furthermore, if a detector channel is missing, the algorithm can compensate for this using weighted data from adjacent LORs so that streak artifacts in the image are avoided. As a result, more weight is given to LORs having a higher number of counts which improves image quality. A problem with MLEM is that it requires more time because multiple iterations must be completed to find suitable image convergence.

Other important concepts are dynamic and gated images. Dynamic images refer to the separation of images into sequential time frames while gated images refer to sampling different phases of physiological cycles such as the cardiac or respiratory cycles. Although the reconstruction methods for these types of images are exactly the same, they result in a time series of images for dynamic data and multiple frames for gated data. The main difference lies in the processing of the data during rebinning. In either case the list mode data contain a time stamp or a physiological marker which can be used to rebin the data prior to reconstruction. The purpose of using dynamic images is

to enable the examination of the kinetics of the tracer in the body, whereas, gated images are generally used to evaluate the pumping function of the heart and to give the appearance of static images in a live animal rather than a blurring over a respiratory cycle, for example.

Chapter 2 – LabPET4™ System Information

2.1. Introduction to the LabPET4™ Scanner

The LabPET4™ system is a PET system dedicated to molecular imaging in small animals, particularly rats and mice. The first version of this system was purchased and installed by the Ottawa Heart Institute in May 2006. In a collaborative agreement with the manufacturer (Advanced Molecular Imaging, Sherbrooke, QC) the Heart Institute agreed to assess the scanner's performance, and to aid in development as there were many elements of the scanner's software and capabilities that needed to be evaluated and expanded upon. The system is based on APDs, which makes it the world's first small animal APD scanner. The LabPET4™ system has the expectation of meeting current standards for small animal PET imaging including high count rate capability, high resolution, and high throughput.

2.2. Avalanche Photodiodes

The scanner is uniquely built on APD technology, a semiconductor based photodetector, which replaces the conventional photomultiplier tubes (PMTs) found in the majority of commercial scanners. APDs are p-n junction diodes generally fabricated from silicon, as is the case for the LabPET4™ scanner. The gamma rays that originate from inside the FOV are converted into near UV light through the scintillation process. The scintillation photons then interact in the depletion layer of the diode creating photoelectrons. By applying a reverse bias voltage, around 200 V, the photoelectrons

will gain enough energy to produce more electrons in a process known as the avalanche effect, resulting in a gain of the signal by a factor of approximately 100-200.

These devices work in proportional mode, thus the total charge collected is proportional to the initial number of light photons impinging on the diode. The light output from the scintillator crystal is directly related to the initial gamma ray energy and directly proportional to the signal obtained from the APD. As a result, the signal acquired from the device can be related back to the original absorbed energy of the gamma ray.

APDs operate analogously to PMTs, are compact, and are less expensive than PMTs making them a suitable choice for a small animal imaging camera. Due to their small size, individual scintillator crystals may be coupled to APDs in contrast to PMT based scanners where a block of crystals would be coupled to one detector. Furthermore, the quantum efficiency of APDs is superior to PMTs with values of 60-80% compared to 15-25% [5]; the quantum efficiency depends on the wavelength of the scintillation light. One considerable drawback to APDs is that they must be operated in very stable temperature conditions and with a stable bias, therefore, small changes in temperature (a few °C) can result in bias and gain variations [26]. The purpose of using APDs in the LabPET4™ scanner is for an improved spatial resolution, compactness, and reduced cost.

2.3. LabPET4™ Specifications

The system utilizes two different types of scintillation crystals including 1536 $\text{Lu}_{0.4}\text{Gd}_{1.6}\text{SiO}_5$ (LGSO) crystals and 1536 $\text{Lu}_{1.9}\text{Y}_{0.1}\text{SiO}_5$ (LYSO) crystals for a total number of 3072 scintillator crystals. Each crystal has a $2 \times 2 \text{ mm}^2$ front face with a length of 10 mm. The crystals are optically isolated and are arranged in a ring like fashion

where a total of 192 detectors are located in each of 16 planes. Each ring is composed of an alternating crystal type as depicted in Figure 2.1. The rings are 16.2 cm in diameter and the total axial FOV (length) of the scanner is 3.75 cm.

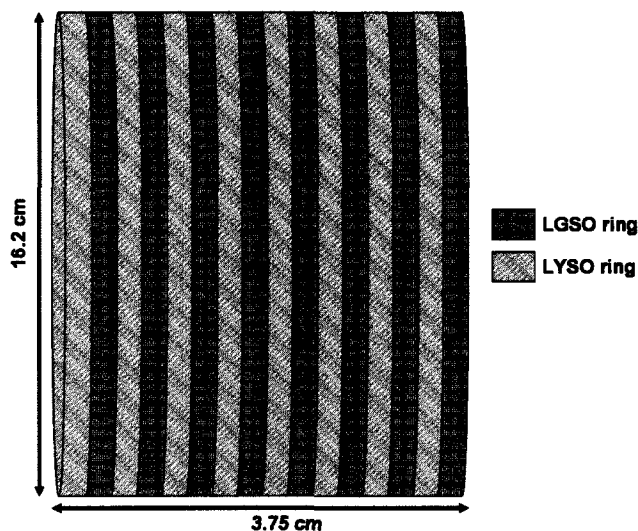


Figure 2.1. Illustration of the alternating rings of different scintillator crystal types in the LabPET4™ scanner.

An LGSO-LYSO pair is coupled to a single APD readout channel in a phoswich pair leading to a total of 1536 detectors channels. The phoswich pair permits individual crystal identification using the dissimilar timing pulse shapes of each distinct crystal type [27]. The energy window is set to 250 – 650 keV for each detector and the overall coincidence timing window is set to approximately 20 ns. The detectors are assembled onto 48 data acquisition cassettes. Each cassette is composed of an analog front end board that is coupled to a digital processing board [28].

The novel LabPET4™ architecture is expected to permit studies in animals on the order of the mouse and rat size. The APD technology allows for quasi-individual crystal coupling that lends itself to an improved spatial resolution since smaller detectors are used leading to more finely sampled spatial information. This is in contrast to PMT based systems where crystal blocks are attached to a single channel [5]. Furthermore, a

highly parallel digital processing architecture allows for a high count rate capability necessary for imaging small animals.

The LabPET4™ system uses a removable ^{68}Ge rotating rod source necessary for normalization and attenuation correction. It also has an integrated vital signs monitor to record temperature, respiratory rate and electrocardiogram (ECG). This feature allows for real-time recording of physiological information so that the reconstructed images may be associated to a certain physiological reference. In addition information such as timing of respiration and cardiac cycles can be utilized to gate the reconstructed images. Remote controlled radiotracer syringe pumps are also incorporated on the system. This facilitates constant rate delivery of radiotracers into a subject and permits for accurate dose delivery. Finally, the LabPET4™ scanner has optional beds and end shield inserts dedicated for mice and rat imaging. The end shields are constructed from lead and sit on the outside of the axial FOV. They help to eliminate out of axial FOV activity, which is expected to decrease scatter contamination. The beds have an appropriate size to fit the end shield for the appropriate animal. The end shields have a diameter of 8.0 and 4.6 cm for rats and mice respectively.

2.4. Data Acquisition, Handling and Reconstruction

The LabPET4™ system is controlled from a graphical user interface running under Mac OS X on an on-board computer. Prior to data acquisition subject and tracer information are entered into the program. The bed is adjusted in order to position the desired organ in the FOV using alignment lasers, and the length of the study is entered. The subject is then injected with the radiotracer and the scan is started.

Data are acquired in a list mode where timing, energy and positional information are recorded. The data can be acquired either in singles mode, where each event is recorded, or in coincidence mode, where events only occurring in the preset timing window are recorded. Using the recorded energy of interaction, the scanner may discriminate against scattered events on the fly. There are two different manners in which data can be acquired on the LabPET4™ scanner. These are known as regular sampling (RS) acquisition mode and double sampling (DS) acquisition mode. The RS mode of operation refers to a stationary acquisition where data are acquired at one fixed bed position in contrast to the DS mode of operation that utilizes axial bed motion. The DS mode of operation is permitted because of the LabPET4™ scanner's unique architecture. Two adjacent crystal rings are coupled to individual APD channels, however, on either side, the crystals are offset by half a detector spacing. This can be envisioned with the aid of Figure 2.2.

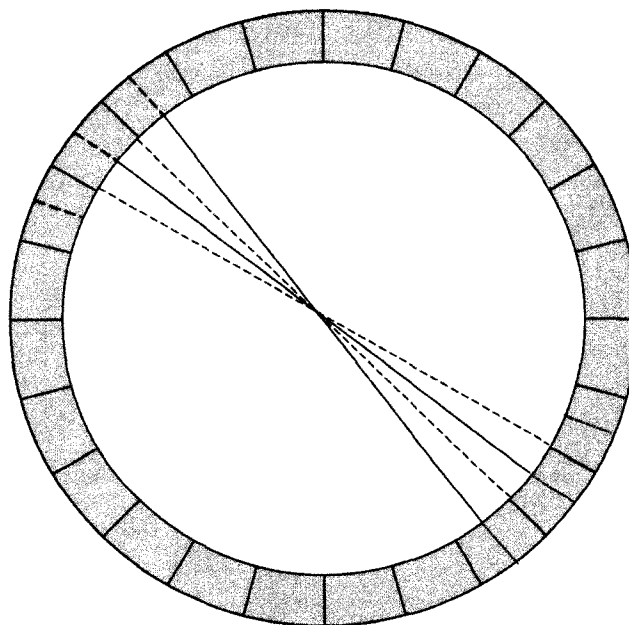


Figure 2.2. The offset detector spacing on the LabPET4™ scanner. The solid lines indicate a plane of detectors and the LORs joining two detectors, while the dashed lines indicate the offset detectors and LORs in the adjacent plane.

Thus, during an acquisition the scanner will acquire data at one bed position, and then the bed will move to the offset plane and acquire data in the new position. The overall effect is to increase sampling density, which is evident from the figure. With a finer spatial sampling, a higher resolution may be obtained.

Once the list mode data are acquired, it is then sorted into a more efficient histogram format using the SSRB technique, as previously described, to allow for 2D reconstruction. The only information preserved at this point is the number of counts and location of the events as the energy and timing discrimination has already been imposed on the coincidence data. The data can then be binned into time frames specified by the user.

There are three different types of histogram files that can be generated consisting of prompt, random and true coincidence histograms. The prompt histograms are all counts that originate from coincidence events within the given timing and energy windows. The randoms histograms are derived from a delayed coincidence window and are subtracted from the prompt histograms to extract only the true plus scattered counts, which are then stored into the true coincidence histograms. For most studies, only the true coincidences are important, however, in some cases the randoms and prompt histograms are used for analysis, as will be discussed in a proceeding chapter. The true coincidence histogram is then accessible for MLEM reconstruction, or it can be reorganized into sinogram format for FBP reconstruction.

The reconstruction algorithms available on the scanner include FBP and MLEM. During the reconstruction process, detector efficiency normalization is employed by specifying an appropriate histogram. The normalization data are obtained using the ^{68}Ge

rotating rod source and are generally acquired during the daily quality assurance test, as discussed in Chapter 3. The FBP algorithm begins by converting the histogram into a sinogram. The sinogram is then back projected utilizing a ramp filter with a default cutoff frequency equivalent to the Nyquist frequency (equation 1.10). MLEM reconstruction is done directly from the histogram and uses detector response modelling to accurately relate projection and image spaces with a system matrix [29], derived from simulation of the LabPET4™ system geometry. The number of iterations to be used is entered by the user prior to reconstruction. For both FBP and MLEM, the scanner has the ability to reconstruct the RS and DS data sets. The RS data reconstruction is for a single bed position, whereas, the DS mode reconstruction uses the multiple bed positions to form a single bed position equivalent.

There are a total of 31 image planes resulting from 16 direct planes and 15 cross planes. With either reconstruction algorithm the span may be adjusted to increase sampling from oblique LORs up to a maximum of 31, which is the physical limit of this scanner. The default span for reconstruction is 3. Each image is circular bounded by diameters of 46, 60, 80 or 100 mm and each pixel in the reconstructed image has a 0.5 mm spacing. The images are saved into digital imaging and communications in medicine (DICOM) format. The final images may then be read and analyzed with PMOD (PMOD Technologies Ltd. Zurich, Switzerland) or MATLAB (The Mathworks, Inc. Novi, MI, USA).

2.5. Available Corrections on the LabPET4™ System

As discussed, the scanner is reportedly capable of correcting for random events using delayed events and detector efficiencies by utilizing the rotating ⁶⁸Ge rod source.

The normalization scan must be acquired daily and an 8 hour scan is recommended by the manufacturer, to permit for sufficient data statistics in order to provide a good detector efficiency correction. Other required corrections for quantitative PET imaging include scatter, attenuation and dead time correction. At the time of this work, no corrections of this type were available, thus the magnitude of these problems must be considered as motivating investigation and discussion in subsequent chapters.

Chapter 3 – Quality Assurance

Daily quality assurance (QA) testing is vital to ensure that an imaging system is operating suitably prior to performing any measurements. When the LabPET4™ camera was purchased, the software to perform this task did not exist, therefore, a solution was necessary. This problem took immediate priority because of its APD technology. As discussed APDs are sensitive to small temperature changes that may result in bias and gain fluctuations, thus the performance can be variable and must be evaluated daily. The objective was to develop a daily protocol that could be implemented easily and automatically so that minimal user intervention was required. The goal was to reconstruct transmission images of a uniform water cylinder to obtain a map of the attenuation coefficients μ . The ^{68}Ge rotating rod source was utilized for this purpose, accompanied by a 250 mL cylindrical Nalgene bottle with a diameter of 6 cm, which was filled with water. In most cases, programs were available to perform the desired tasks; however, in some cases, software was altered or new software was introduced. The entire process was programmed to run daily using a Unix shell script.

The first step in the protocol was to obtain a blank scan. This was achieved by letting the rod source rotate while in acquisition mode for 8 hours without any object present in the FOV. This scan was not only available for the QA but also became the normalization which was needed on a daily basis for all acquisitions due to the temperature sensitivity of the system. The next step was to obtain a transmission scan of the water cylinder. This was achieved by moving the bed axially with the water cylinder on board so that the water cylinder was positioned in the center of the FOV. A 2 hour

acquisition was then obtained with the rotating rod source. The list mode data were subsequently rebinned into histograms using the available system software.

Once the data were acquired and binned, the counts were converted to count rates. Attenuation correction factors (ACFs) were then obtained following equation 1.6. The ACFs will be discussed in more detail in Chapter 5. Rearranging equation 1.6 we can obtain the ACF for each LOR by:

$$ACF_{r,\theta} = \frac{I_{o,r,\theta}}{I_{r,\theta}} = e^{\int u_{r,\theta}(L)dL} \quad (3.1)$$

where I_o represents the blank scan, I represents the transmission scan of the water filled cylinder, and L is the distance a gamma ray passes through an object with attenuation coefficient μ . The exponent is analogous to the emission projections $g(r,\theta)$ of equation 1.8 for an activity distribution $f(x,y)$ where $f(x,y)$ is replaced by $\mu(x,y)$ for transmission imaging. Therefore, by taking the natural logarithm of equation 3.1 the following relation can be established for each LOR:

$$g_{r,\theta} = \ln(ACF_{r,\theta}) = \int \mu_{r,\theta}(L)dL \quad (3.2)$$

which is the same as equation 1.8 for a fixed radius r and angle θ . If all possible LORs $g(r,\theta)$ are considered, the following relation can be written:

$$\mu(x,y) = FBP[\ln(ACF(r,\theta))] \quad (3.3)$$

which is a reconstructed image of the attenuation coefficients per pixel. To obtain the attenuation coefficient in units of cm^{-1} , the attenuation coefficients are divided by the image pixel size of 0.05 cm/pixel.

The ACFs were obtained simply by dividing each histogram bin in the blank scan by each respective bin in transmission data to form a new histogram. The natural

logarithm of the resulting histogram was then computed. Programs were written to perform both of these tasks. MLEM reconstruction with 6 iterations was then used to reconstruct the logarithm histogram. 6 iterations were chosen as a standard based on visual image analysis from multiple daily QA scans. The data have poor count statistics, thus a higher number of iterations would amplify the noise resulting in uninterpretable images. Furthermore, due to the incomplete development of the MLEM algorithm on the scanner it was not possible to quantify the reconstructed transmission images as part of the protocol, therefore, only the logarithm of the ACFs were reconstructed. FBP could not be used as an alternative, again because of limited data statistics. All operations described above were incorporated into a Unix bash shell script that was programmed to run daily. The only user intervention required was to ensure that the water cylinder was placed on the bed in a predefined location and that the ^{68}Ge rod source was inserted into the scanner. Example reconstructed images are shown in Figure 3.1. This figure shows two images for both a successful and failed QA. The top left picture shows a transaxial slice that is accompanied by coronal and sagittal slices of the image to the right and bottom respectively. The greyscale image is the maximum intensity projection (MIP) which gives the pixel of greatest intensity through all planes. The black/red colors represent regions of lower intensity, while the yellow/white regions represent regions of higher intensity.

The QA image was manually reviewed on a daily basis using PMOD prior to commencing any measurements on the scanner. If there were no visible artifacts in the image, as shown in Figure 3.1(a), the scanner passed the QA. An axial banding pattern was observed on the MIP in all cases and was attributed to higher noise recorded in the

LGSO direct planes due to relatively low sensitivity compared to LYSO planes. In the second case, a failed QA was identified when an image artifact was encountered. An example of this is shown in Figure 3.1(b). Here it was noticed that there was streak artifacts on one of the transverse planes and bright spots in the MIP. The artifact in this

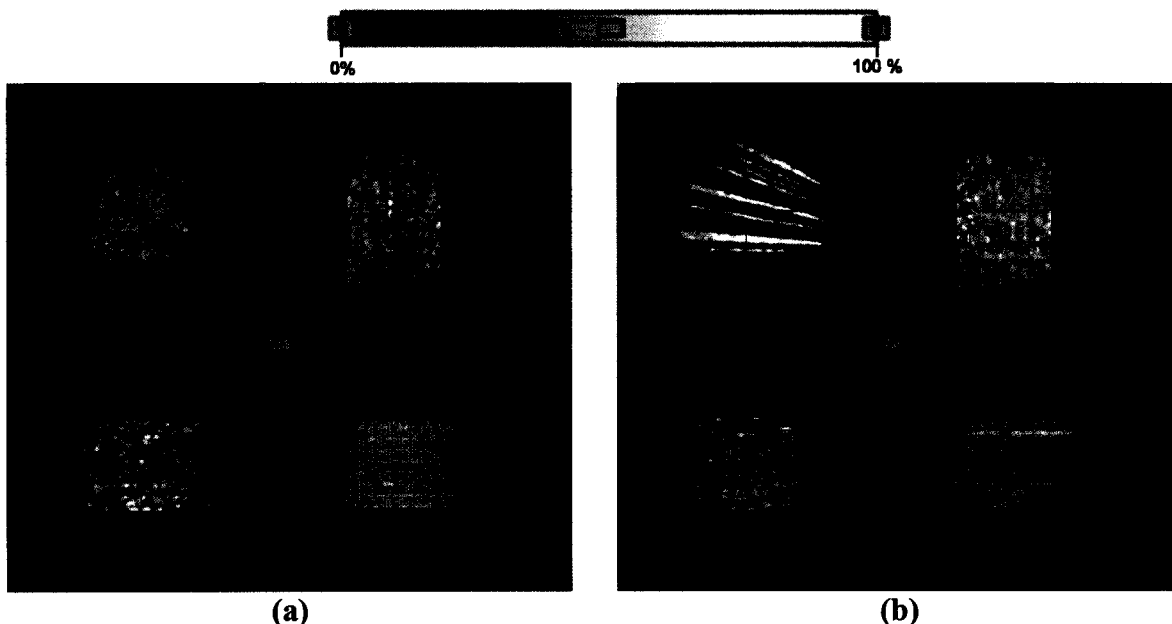


Figure 3.1. Reconstructed transmission images of a 250 mL Nalgene bottle demonstrating (a) a successful QA (b) a failed QA.

case was due to an APD operating incorrectly which translated into abnormal counting from this channel. Consequently, its bias voltage needed to be adjusted. This artifact suggests that a variation had occurred during the QA process so that the blank and transmission scans were acquired when the scanner was operating in different states with a different number of detectors working. If an emission scan was done later in that day, the blank scan, used for normalization, would not match these data because they were not acquired while the scanner was in the same state and this artifact would translate into the emission data. From the figure it was noticed that the streaks originate to a focal spot which identifies the bad detector channel. Other problems may also occur including extremely noisy images or the recording of no image. These problems suggest that an

error has occurred in the scanner hardware or software, and in these cases it can be more difficult to diagnose the origin of the problem.

The images were further analyzed on a daily basis to compute the mean, maximum and minimum pixel values within the central region (4.5 cm in diameter) of the phantom. The corresponding standard deviation was also computed and the ratio of the standard deviation to the mean was also computed in order to assess the noise in the images. These quantities were plotted versus time, and are shown in Figure 3.2 for a one-month period.

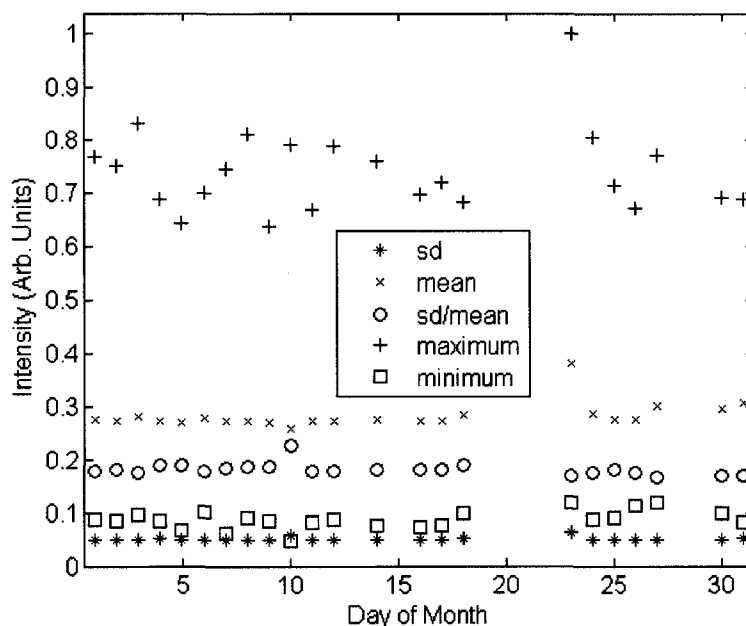


Figure 3.2. Plot of statistics for the QA transmission images acquired over one month. The mean, standard deviation, maximum value, minimum value and the ratio of the standard deviation to the mean are plotted over the day of the month.

The ratio of the standard deviation to the mean shows a relatively constant value with the exception of day ten where an increased value was observed. This signifies a noisy image and it was also noted that a slight increase in the standard deviation was recorded with a small minimum value. Because this value appeared to be outside of the observed

trend, the scanner was deemed unsuitable to perform imaging on that day because it was expected that the noise could appear in the emission data. Another outlier point was observed at day 23, where the maximum and mean values were above the trend observed. This point was due to streak artifacts as illustrated in Figure 3.1 (a). Again, these data suggest that a problem occurred and that the daily QA image should have been examined closely to determine if the scanner was capable of performing emission imaging on that day. There were also absences of points on certain days. These were due to the scanner not completing the QA task, therefore, these cases were regarded as an unsuccessful QA. In the event of any unsuccessful QA, the manufacturer was contacted immediately to identify the problem. If an APD problem had occurred, the manufacturer could adjust the APD bias remotely using the information presented from the QA. If a more critical error had occurred, the QA image could be used to make an initial guess as to the origin of the error.

Due to the incomplete development of the MLEM reconstruction algorithm, the attenuation coefficients could not be reconstructed with units (eg. cm^{-1}). An alternative approach was thus taken to estimate the attenuation coefficients. In this case, the histograms were transformed into sinograms with a span of 31 so that all of the 3D data were utilized. The data were then imported into MATLAB and all sinograms were added into one plane, exploiting the axial symmetry of the phantom. The logarithm was taken following the division of the sinograms and then the data were divided by the pixel size. The *iradon* (*inverse radon*) function was used to reconstruct the data via FBP (equation 1.10) in MATLAB. A region of interest encompassing the central 4.5 cm in diameter of the phantom was drawn, and the average pixel value of this region was computed along

with the standard deviation. A value of $\mu = 0.065 \pm 0.010 \text{ cm}^{-1}$ was calculated. From Table 1.2 we see that the actual narrow beam attenuation coefficient of soft tissue is 0.096 cm^{-1} , which is identical for water. The values were not comparable in this case, however, from Table 1.2 it was observed that the attenuation coefficient is dominated by the contribution of Compton scatter. As a result, scattered photons will be produced within the object and will be detected in the transmission data. This will reduce the measured attenuation coefficient due to photon buildup.

Daily quality assurance is a vital component for assessing the LabPET4™ performance on a day to day basis to ensure that the scanner is capable of measuring emission data. This preliminary QA demonstrates its ability to assess the scanner's performance, and further analysis reveals that estimation of the attenuation coefficients is possible. It is expected that the manufacturer will introduce improvements that will be implemented on the scanner to enhance the data statistics and allow for estimation of the attenuation coefficients using MLEM.

Chapter 4 – Performance Evaluation of the LabPET4™ Camera

4.1. Motivation

The LabPET4™ camera is new to the commercial market and incorporates an innovative APD technology. Because this technology is still in its infancy, the scanner's performance needs to be evaluated to certify that it meets the manufacturer's specifications and to assess its ability for small animal imaging. The main goals of this section can be divided into the three following questions:

- (a) What is the optimal activity we should inject for a given animal size?
- (b) Are dead time, scatter and attenuation corrections necessary?
- (c) Does this camera have the capability for cardiac imaging and quantification of physiological processes in small animals?

To answer these questions the system's absolute sensitivity, scatter fraction, noise equivalent count rate, dead time, reconstructed image resolution, image non-uniformity, scatter and attenuation are examined. Finally, cardiac images of a rat and mouse are investigated to confirm the camera's ability for small animal cardiac imaging. The expected specifications from the manufacturer are shown in Table 4.1.

Table 4.1. Expected system specifications for the LabPET4™ scanner

Quantity	Specification
Sensitivity	1%
Peak Noise Equivalent Count Rate	1 Mcps
Quantitative Accuracy	> 95% (up to Peak Count Rate)
Resolution	< 1.4 mm

4.2. System Absolute Sensitivity

The sensitivity is an important measurement because it quantifies the ability of the scanner to convert positron decay in the FOV into true counts. For this experiment, approximately 100 μL of an ^{18}F solution (4.2 MBq) was placed into a small thin-walled (0.5 mm) plastic vial. The vial was then positioned in the center of the axial and transverse FOVs. The small volume of activity and thin walls ensured that scatter and attenuation were negligible so that these factors did not reduce the count rate. The low activity ensures that random and dead time effects could be neglected. For this study, it was assumed that all of the positrons annihilated and produced gamma-ray pairs. Moreover, the positioning of the vial in the center of the scanner optimized the geometric aperture. A short acquisition of 300 seconds was performed and the data were stored in list mode format.

The raw data from the acquisition were rebinned into histogram format and a total count report was automatically generated in the process. The count rate report generated the prompt counts, random counts and true counts. The true counts (N_t) that corresponded to a 100 mm diameter FOV with a span 31 were extracted so that all possible counts originating within the FOV were counted. The expected number of positron decays (N_{exp}) was then calculated with knowledge of the initial activity (A_o), the branching ratio, and the half life ($t_{1/2}$) using the following relation:

$$N_{exp} = 0.97 \int A(t) dt = \int_0^t A_o e^{-\lambda t} dt \quad (4.1)$$

where 0.97 is the branching ratio of positron decay for ^{18}F [5], and λ is defined by:

$$\lambda = \ln(2) / t_{1/2} \quad (4.2)$$

The sensitivity was then calculated by taking the ratio of the measured true counts divided by the expected number of true counts:

$$\text{Sensitivity} = \frac{N_t}{N_{\text{exp}}} \times 100 \% \quad (4.3)$$

and this value was found to be 0.57% which was low in comparison to the specification of 1%. This problem should therefore be addressed by the manufacturer.

The value here is quoted for the center of the axial and transverse FOVs and is only applicable to this point inside the scanner. Therefore, this measurement gives us the optimal efficiency for conversion of positron decay into true counts at this particular point. Additionally, line source measurements can be done in order to obtain sensitivity profiles over the axial extent of the scanner. A method for doing this is discussed by the Animal Standard Task Force [30]. Following the standard a 15 cm tube filled with an ^{18}F solution is used. The line source is placed in five concentric Aluminum sleeves, each having the same small wall thickness (ie. 2.5 mm). An acquisition is completed, then one of the sleeves is removed and another acquisition is started. This is continued until only one sleeve is left. The sensitivity for each image plane is then calculated, taking into consideration the branching ratio and radioactive decay of the isotope, and is plotted versus the number of sleeves. This plot is fitted to an exponential function and extrapolated to a zero wall thickness to obtain the axial sensitivity profile. The absolute system sensitivity is then calculated as the average sensitivity over all planes. The value at the center of the profile corresponds to the point source measurement as discussed in this section.

The method defined in the standard ensures that all of the positrons are absorbed in the medium since Aluminum is used, and it also accounts for attenuation because of

the extrapolation technique. In comparison to the point source sensitivity measurement presented in this section, the plastic vial used had a 0.5 mm wall thickness and the maximum and mean positron ranges for ^{18}F in tissue are 2.3 mm and 0.35 mm, thus it is possible that some of the positrons were not absorbed in the point source measurement. Although it was assumed that all positrons converted to gamma ray pairs, the line source measurement method ensures that this in fact occurs. The line source measurement should thus be performed in future work.

4.3. Noise Equivalent Count Rate and Scatter Fraction

An overall reconstructed image quality assessment is a vital component for quantifying an imaging system's performance. To perform this measurement, the signal to noise ratio (SNR) of a reconstructed image may be obtained by measuring a PET scanner's noise equivalent counts (NEC). The noise equivalent counts can be thought of as the equivalent true events in the absence of scattered and random events. Scattered and random events do not contribute to the desired signal in the image, but they do introduce noise. The two quantities, NEC and SNR, are related directly through the following relationship for a uniform cylindrical image reconstructed with FBP:

$$NEC \propto SNR^2 \quad (4.4)$$

This equation is derived based on Poisson counting statistics where the variance (σ^2) is equal to the mean count rate (μ). We can then write the SNR as:

$$SNR = \frac{\mu}{\sqrt{\sigma^2}} \propto \frac{T}{\sqrt{T + S + R}} \quad (4.5)$$

where T, S and R are the true, scattered and random events respectively. The NEC for a PET system was initially shown in [31] and it takes the form:

$$NEC = \frac{T^2}{T + S + afR} \quad (4.6)$$

The factor f is the fraction of the sinogram width that the object subtends radially. This factor is used to ensure that only the random events recorded within the object are used in the NEC calculation. The factor a is incorporated to take into consideration the type of randoms correction that is imposed on the data. If the randoms are estimated by singles events, then the factor takes the value of unity, whereas if the randoms are corrected using a delayed window technique, the factor becomes two because there is twice as much noise introduced into the data. The NEC is only an estimate of the global SNR and does not account for localized variations in the activity distribution [5].

The critical factors in determining the NEC are the geometry that is employed and the activity that is present inside the FOV. The geometry is what governs the overall fraction of the total (randoms corrected) counts that exist as scatter, known as the scatter fraction (SF), which depends on the scanner's geometry (ie. gantry, detectors) and the object that is placed in the FOV. Ideally, the activity in the FOV is directly related to the true event rate, however, increasing the activity will also increase the randoms rate and system dead time which both limit the NEC.

Since the original presentation of the method for measuring NEC, standards have been developed in order to provide a comprehensive approach for comparing NEC curves from different PET systems along with other performance measures [32]. Furthermore, since the advent of small animal PET imaging systems, there has been a growing interest in introducing a standard for comparison of these scanners. This has been a recent topic of discussion by the Animal PET Scanner Task Force and a version of the proposed testing procedure is currently available [30].

The LabPET4™ scanner was evaluated using the small animal PET procedure to obtain the NEC and the SF using mouse-like and rat-like phantoms. Both phantom designs were taken from the Animal PET Scanner Standard and were assembled out of high density polyethelene ($\rho = 0.96 \text{ g/cm}^3$). A tube that was made of a clear flexible plastic, with an outer diameter of 3.2 mm and an inner diameter of 1.6 mm, was filled with activity and inserted into the phantoms. The rat-like and mouse-like phantoms had the same cylindrical geometry with different dimensions. The mouse-like phantom was 7 cm in length and 2.5 cm in diameter with a 3.2 mm hole drilled off axis at 1 cm for insertion of the tube. In contrast, the rat phantom was 15 cm in length with a 5 cm diameter and a 3.2 mm hole drilled off axis at 1.75 cm. The tubes had a length that was 1 cm shorter than the length of the phantoms. The rat-like phantom is illustrated in Figure 4.1.

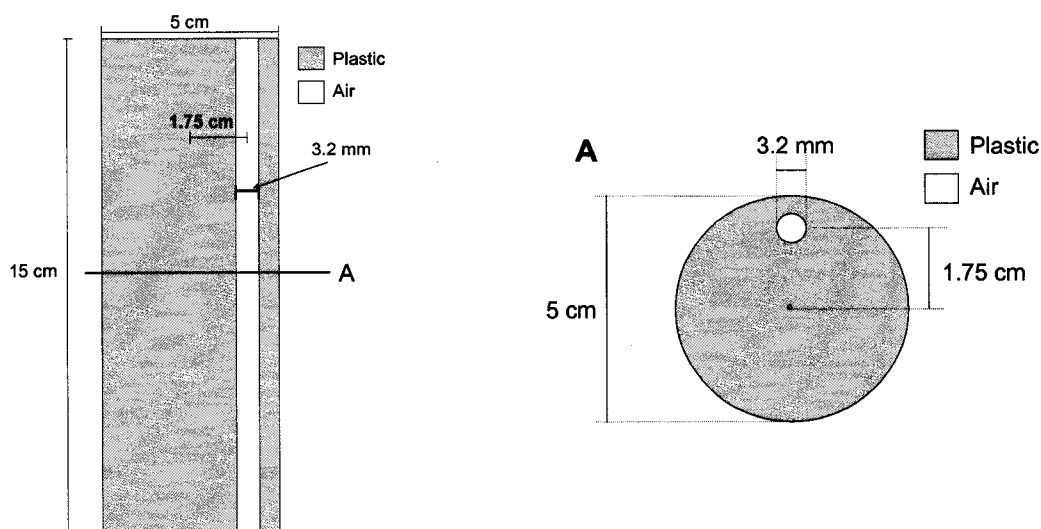


Figure 4.1. Rat phantom design for NEC and SF evaluation following the Animal PET Scanner Standard [30].

For both cases, a ^{11}C solution was injected into the tube, which was then inserted into the central region of the phantoms. For the mouse study an initial activity of 280 MBq was injected, while 555 MBq was used for the rat study. The phantom was

centered in both the axial and transverse FOVs and the rat end shield insert was used in each study. The activity was then allowed to decay for 195 minutes and 200 minutes for the mouse and rat studies respectively. The initial activity was high in these studies to create an appreciable scanner dead time and to ensure that the peak NEC rate was reached, as called for in the protocol. Furthermore, a long scan was obtained to incorporate a range of activities and so that the random event rate at the end of the scan was only a small fraction of the true event rate ($\sim 1\%$), again following the standard.

The data were rebinned into prompt and random count histograms occurring in 5 minute intervals. The randoms data were measured using the available delayed window technique included with the scanner's software. The data were then reorganized into the corresponding prompt and random sinograms having a total of 240 projections and 0.5 mm pixels radially. The sinograms did not include any corrections for normalization, dead-time, scatter or attenuation. A span of 31 was used with a 100 mm field of view to incorporate all of the data stored in the histograms. A total of 39 time frames, each with 31 image planes, were reorganized into sinograms for the mouse-like phantom, and 40 x 31 for the rat-like phantom data. All bins that were located further than 8 mm radially from either side of the rat-like and mouse-like phantoms were first set to zero in both the prompt and random sinograms. Each sinogram was then summed over all angles to obtain one profile that corresponds to the number of counts versus radial bin. Due to the phantom geometry, with the tube insertion hole drilled off axis, the sinogram data must be aligned before summing over all angles. This was obtained by aligning the peak values in each angular projection prior to applying the sum operation.

The next step was to partition the prompt sinograms into a random plus scatter background accompanied by the true counts. A 14 mm band was assigned around each summed profile's maximum intensity pixel and the values occurring at ± 7 mm were recorded. The average of the two values was calculated and multiplied by the number of pixels to obtain the random and scatter background within the band. The pixels outside this region were then added to the random and scatter events as it is known that these events do not contribute to the true events. The partitioning is illustrated in Figure 4.2. Furthermore, the total events were also calculated by summing the total events in the profiles.

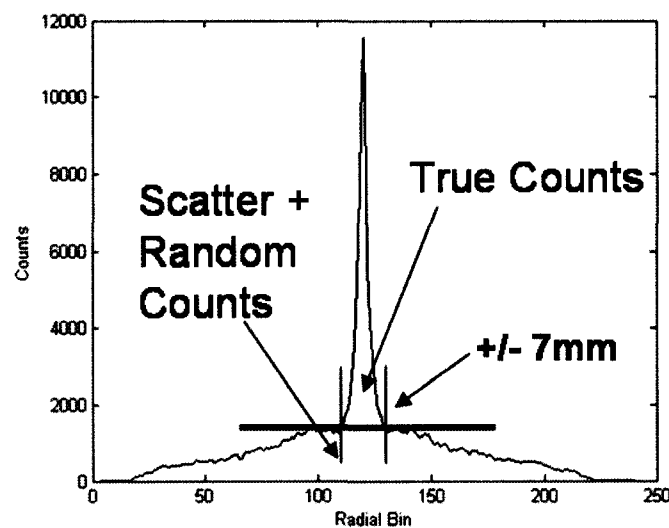


Figure 4.2. A summed profile of the aligned prompt data illustrating partitioning of the counts into true and random plus scatter background.

After the partitioning was completed, information such as the scatter fraction, total event rate, true event rate, random event rate, scatter event rate and NEC rate could be obtained. The scatter fraction is an essential calculation because it gives an estimate of the fraction of the total events that have undergone scatter for mouse-like and rat-like geometries. The overall scatter fraction for the phantoms is defined by [30;32]:

$$SF = \frac{\sum_i \sum_{j'} C_{r+s,i,j'}}{\sum_i \sum_{j'} C_{TOT,i,j'}} \quad (4.7)$$

where C_{r+s} are the random plus scatter background counts, C_{TOT} is the total counts in a summed profile, i is the image plane number and j is the frame number with the prime denoting the later time frames when random events and dead time are assumed to be negligible; this occurs at approximately 200 minutes in each case. In the last 5 time frames, for the rat-like phantom measurement, the randoms rate was found to be less than 2% of the trues, while for the mouse-like phantom measurement the randoms rate was below 1%. It was actually required that the randoms rate be below 1% for this measurement following the protocol, therefore a problem was noted with the randoms background for the rat-like phantom and this will be addressed at the end of the section. With equation 4.7 the scatter fraction was estimated to be 22.4% and 28.4% for the mouse-like and rat-like phantoms respectively. This calculation gives insight into how many of the total counts, neglecting randoms, we would expect to be in the form of scatter if we were to image an animal on the order of the size of the phantoms.

The total, true, random, scatter, and noise equivalent count rates were then calculated and plotted against the average activity for each time frame in order to view all of the different count rates separately. The average activity for a time frame j of length T_{acq} is defined by [30;32]:

$$A_{ave} = \frac{A_0}{\ln 2} \left(\frac{T_{1/2}}{T_{acq}} \right) \left\{ 1 - \exp \left(\frac{-T_{acq}}{T_{1/2}} \ln 2 \right) \right\} \quad (4.8)$$

where A_0 denotes the starting activity at the specific time frame, and T_{acq} was five minutes. The total event rate and the random plus scatter count rate were calculated by

summing all counts over planes i then dividing by T_{acq} , while the true event rate for frame j was extracted by [30;32]:

$$R_{t,j} = \sum_i R_{t,i,j} = \sum_i \frac{C_{TOT,i,j} - C_{r+s,i,j}}{T_{acq}} \quad (4.9)$$

Furthermore, the random event rates, $R_{r,i,j}$, were calculated using the total counts available in the delayed random sinograms then by dividing by the acquisition time. The scatter event rate for time frame j was then calculated using [30;32]:

$$R_{s,j} = \sum_i \left(\frac{SF_i}{1 - SF_i} \right) R_{t,i,j} \quad (4.10)$$

where SF_i denotes the scatter fraction of plane i ; this was obtained through removal of the sum over i in equation 4.7. Finally, the NEC rate was obtained utilizing the true event rate, the total event rate and the random event rate [30;32]:

$$R_{NEC,j} = \sum_i \frac{R_{t,i,j}^2}{R_{TOT,i,j} + R_{r,i,j}}. \quad (4.11)$$

The total rate plus the randoms rate was adopted in the denominator because the scanner corrects for random events using a delayed window, thus the factor a is two from equation 4.6. If a was equal to one, the factor $R_{r,i,j}$ would disappear in the equation. All of the discussed count rates are plotted in Figures 4.3 and 4.4 for the mouse-like phantom and rat-like phantom respectively as a function of the average activity of each time frame.

The count rates presented in Figures 4.3 and 4.4 give an appreciation of all the available count rate data. Note that all of the rates increase to a certain point, then begin to decrease suggesting random events and system dead time begin to dominate. The most important rates to take into consideration are the NEC rates and these curves are plotted separately in Figures 4.5 and 4.6 for each phantom.

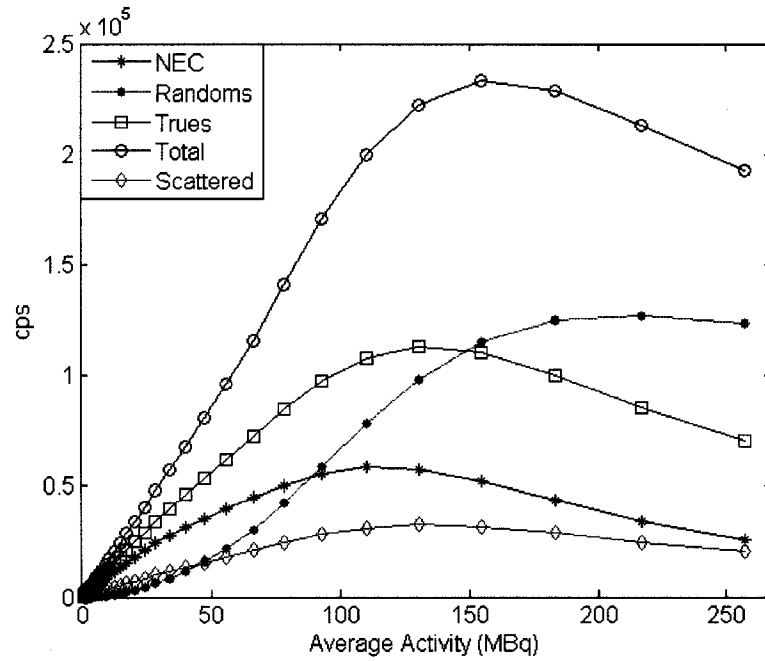


Figure 4.3. Plot of the different count rates for the mouse-like phantom as a function of the average activity over the time interval.

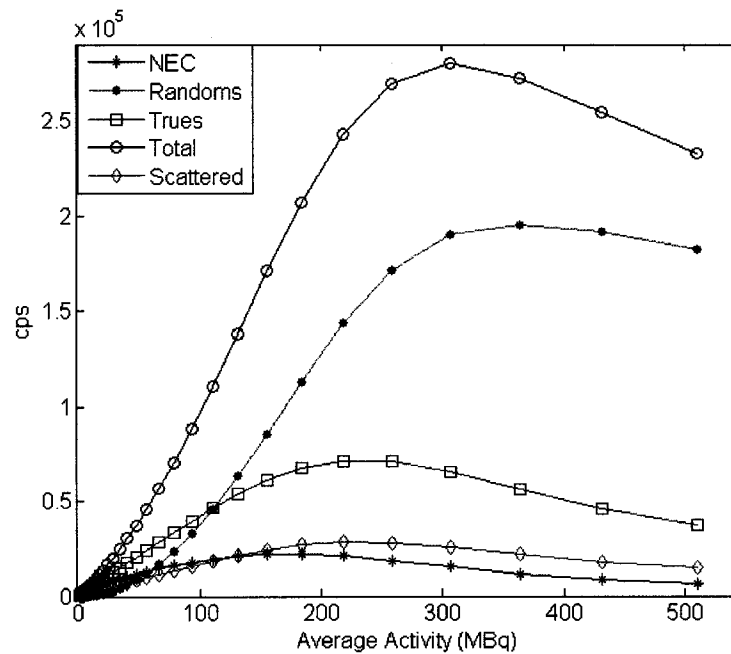


Figure 4.4. Plot of the different count rates for the rat-like phantom as a function of the average activity over the time interval.

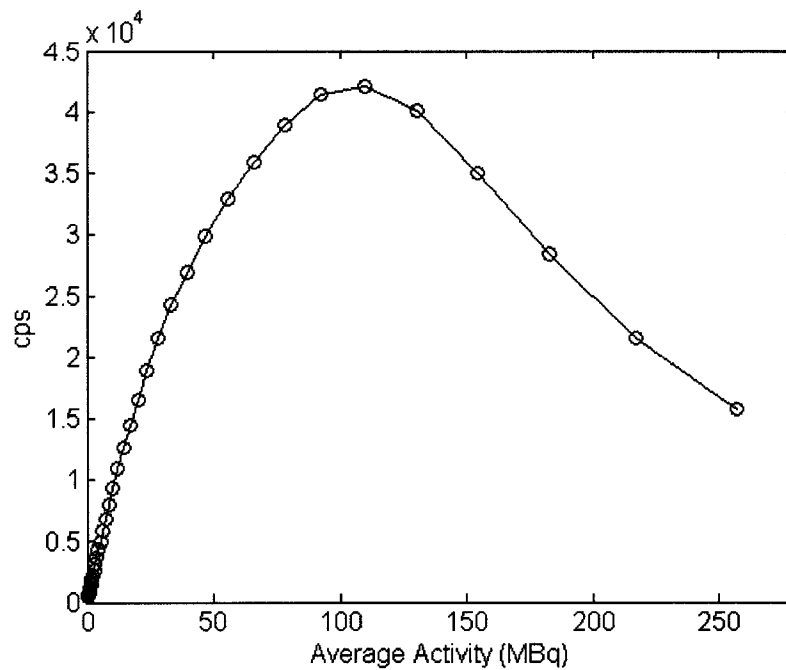


Figure 4.5. An expanded view of the NEC curve for the mouse-like phantom. The peak NEC occurs at 110 MBq with a peak of 42.0 kcps.

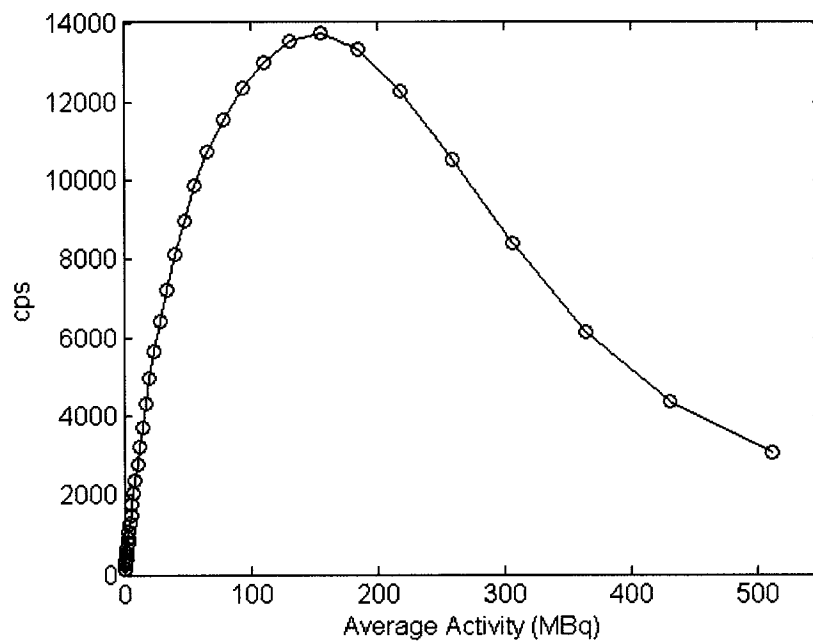


Figure 4.6. An expanded view of the NEC curve for the rat-like phantom. The peak NEC occurs at 156 MBq with a peak of 13.7 kcps.

Both curves have similar shapes with an increasing NEC up to a peak, then a decrease afterwards. The peak NEC is associated with an activity that produces the highest SNR in the image for a geometry similar to the phantoms. The peak NEC rate for the mouse-like phantom was 42.0 kcps occurring at 110 MBq. For the rat-like phantom the peak is observed at 156 MBq with 13.7 kcps. Thus, when imaging a mouse or rat, these approximate activities are expected to produce images with the highest quality. The decrease in NEC following the peak is due to the random event rate rising quickly with the square of the activity as is noticed in Figures 4.3 and 4.4. Additionally, all of the count rates are found to decrease, especially the trues, which are directly related to the system dead time as discussed in the next section.

During these calculations, a bias in the measured delayed random event rate was encountered upon comparing these values to an analytical calculation [30;32]:

$$R_{r,j} = \sum_i R_{r,i,j} = \sum_i R_{TOT,i,j} - \left(\frac{R_{t,i,j}}{1 - SF_i} \right) \quad (4.12)$$

At the peak NEC the measured randoms were found to be overestimated by 28% for the mouse-like phantom and 21% for the rat-like phantom. To understand the effect of the bias on the NEC, the analytic random calculation was used in place of the delayed randoms measurement in equation 4.11. The new peaks were 44.8 kcps at 110 MBq for the mouse-like phantom and 14.6 kcps at 185 MBq for the rat-like phantom. These had an increase of 6.7% and 6.6% respectively suggesting improvements in image quality can be obtained with an accurate delayed window randoms correction implemented on the scanner. Furthermore, the bias in the randoms helps explain why the randoms rate was not less than 1% of the trues at low activity for the rat-like phantom experiment.

LYSO and LGSO in the LabPET4™ system contain some intrinsic radioactivity due to ^{176}Lu which decays by beta minus decay, thus a constant background will be introduced into the data set in the form of randoms and true events where the true events are a result of cascading gamma rays [33;34]. An alternative method for estimating the scatter fraction was therefore proposed to account for this intrinsic background rate [33;34] and is adopted by the Animal PET Scanner Standard [30]. The intrinsic background will introduce additional true counts from the cascading gammas and this will bias the scatter fraction calculation presented in equation 4.7. The standard requires measurement of the scatter event rate to be obtained with [30]:

$$R_{s,i,j} = R_{Tot,i,j} - R_{t,i,j} - R_{r,i,j} - R_{int} \quad (4.13)$$

where R_{int} is the intrinsic true rate. R_{int} was measured on the LabPET4™ by taking a short acquisition without any activity in the FOV as 28 cps. However, it was found that at higher activities (ie. 180 MBq for the rat-like phantom measurement) that the scatter event rate using equation 4.13 became negative because of the overestimated randoms. Due to the negative scatter event rate recorded, the scatter fraction could not be obtained by this method. Instead, to understand the bias in the scatter fraction, equation 4.7 was adjusted to subtract the intrinsic true rate from the scatter and prompt event rates. The new scatter fractions recorded were 22.1% and 28.0% with the intrinsic true rates taken into consideration, and upon comparison to the 22.4% and 28.4% recorded for the mouse-like and rat-like phantoms, only a small change was noted. It was concluded that the intrinsic true rate in fact alters the scatter fraction measurement, but only by a small fraction.

The values calculated for the peak NEC were a factor of 20 lower in comparison to the quoted values from the manufacturer of ~ 1000 kcps for a mouse-like phantom. This would decrease the SNR by a factor of $\sqrt{20}$ leading to reduced image quality. To achieve the expected NEC quantities, issues such as the sensitivity, randoms and dead time would need to be addressed. If the sensitivity was increased, due to improved coincidence timing for example, the true event rate would increase and the coincidence timing window could also be shortened leading to the rejection of more random events. Through an increased true event rate and decreased random event rate, the NEC would inevitably increase. To determine the activity required to reach 1000 kcps, an ideal NEC calculation can be considered by neglecting the random and scatter contributions. In this case the NEC would be proportional to the true event rate. Thus, taking into account the 0.6% sensitivity, 160 MBq would need to be injected to obtain the desired NEC. However, in practice, this rate is ultimately limited by dead time as will be apparent from the discussion in the next section.

Finally, a proper randoms correction would lead to an increased NEC as discussed, however, randoms correction from singles using equation 1.7 could also be used so that the factor a would be unity in equation 4.6 and the randoms would contribute less noise in the measurement (ie. the factor $R_{r,ij}$ would be dropped in equation 4.11). This was verified through updating equation 4.11 and proceeding with the NEC calculation. This computation yielded 22.1 kcps at 180 MBq for the rat-like phantom and 58.4 kcps at 110 MBq for the mouse-like phantom. The NEC would increase by 50% for the rat-like phantom and by 30% for the mouse-like phantom.

4.4. System Dead Time

As discussed in Chapter 1, the system dead time will limit the maximum count rate that can be recorded by producing nonlinear count losses at high activities. At a particular activity, the count rate may begin to decrease with increasing activity. To quantify the dead time of the system, the true event rates are studied from section 4.3 for the mouse-like and rat-like phantoms. As was noted from Figures 4.3 and 4.4, the true rate increases linearly at lower activities and then decreases at higher activities. These data have been corrected for both random and scatter events, suggesting the origin of the decrease was from dead time losses. The linear portion of the true rate, which occurred at lower activity, was fitted to a straight line using linear regression. This occurred below 4 MBq for the mouse-like phantom and below 50 MBq for the rat-like phantom. The true event rates are plotted versus average activity in Figures 4.7 and 4.8 for the mouse-like and rat-like phantoms respectively, and are accompanied by the ideal true rates as measured by the linear fit. Furthermore, the percentage dead time at a particular average activity was then calculated by:

$$\text{percentage dead time} = 100 - \frac{\text{measured trues}}{\text{ideal trues}} \times 100\% \quad (4.13)$$

The percentage dead time for each phantom is presented in Table 4.2 for various activities and is also plotted as a function of activity in Figures 4.7 and 4.8.

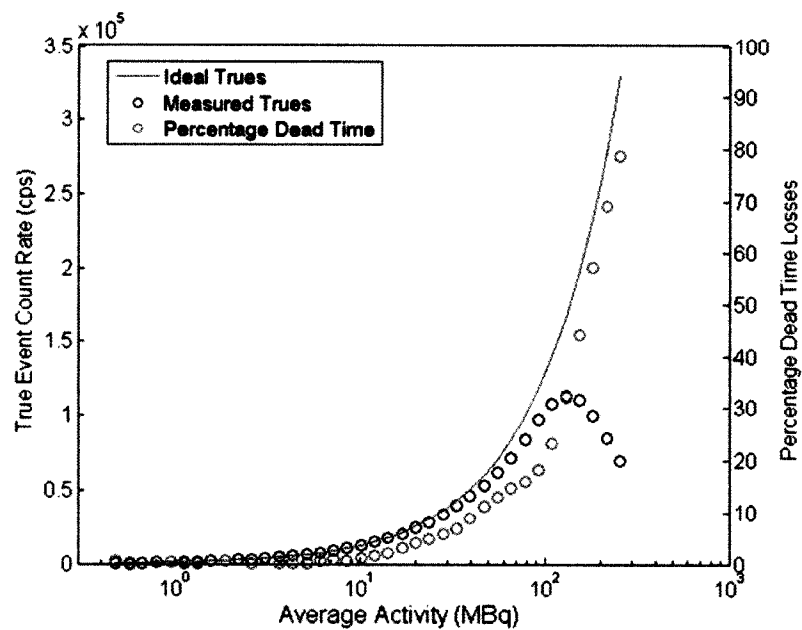


Figure 4.7. Comparison between the measured true rate (blue) and the ideal true rate (red) as a function of average activity for the mouse-like phantom. The percentage dead time losses (green) is also plotted versus the average activity.

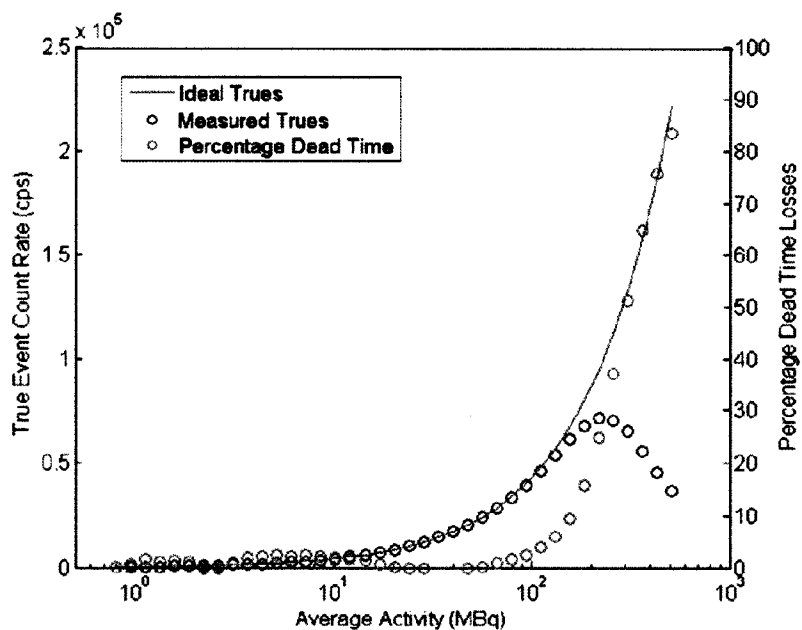


Figure 4.8. Comparison between the measured true rate (blue) and the ideal true rate (red) as a function of average activity for the rat-like phantom. The percentage dead time losses (green) is also plotted versus the average activity.

Table 4.2. Percentage dead time for the mouse-like and rat-like phantoms.

Percentage Dead Time	Average Activity (MBq) Mouse-Like Phantom	Average Activity (MBq) Rat-Like Phantom
2	12	85
5	24	120
10	42	155 (peak NEC)
25	110 (peak NEC)	220
50	160	300

The data presented support the need for a dead time correction on the LabPET4™ scanner. As can be seen, dead time limits the peak count rate and is non-negligible around the peak NEC. A dead time correction would allow for the adjusted trues to vary linearly with increasing activity, thus permitting for quantitative accuracy with a wider range of injected activity. The percentage dead time presented in Table 4.2 gives an estimate of the quantitative accuracy in a mouse and rat like object. The data suggest that if a mouse or rat was imaged with activities less than 24 MBq or 120 MBq respectively, the inaccuracy would be limited to within 5%. At even higher activities, the dead time increases and ultimately limits the quantification that could be obtained with the scanner. In conclusion, a dead time model should be developed to correct for this phenomenon or the system dead time reduced (eg. by decreasing the coincidence timing window).

4.5. Reconstructed Image Resolution

The reconstructed image spatial resolution for a scanner is an important quantity because it gives the physical limit of how closely two objects can be placed inside the scanner but still be distinguished. The LabPET4™ system has the potential of high resolution, due to the incorporation of the quasi individual crystal coupling, to allow for small animal imaging. Typically, measurements of reconstructed image resolution are obtained following the NEMA protocol [32] where concentrated activity is placed inside

a point source and then positioned at six different points inside the scanner's FOV. The acquired data are then reconstructed using filtered backprojection and the system response function is examined to determine the FWHM, which is reported as the image resolution. In contrast, iterative reconstruction methods are becoming the standard in PET and MLEM is the standard method for reconstruction on the LabPET4™ system. A suitable method for measuring the reconstructed transaxial image resolution was therefore proposed using MLEM with a more realistic imaging scenario (ie. a 5 cm diameter phantom instead of a point source) [1].

The reconstructed image resolution measurement data were obtained using a Micro Deluxe Phantom™ (Data Spectrum, Hillsborough, NC, USA) with a “hot rods” insert having diameters and spacings of 4.8, 4.0, 3.2, 2.4, 1.6 and 1.2 mm for each respective hole. The phantom container had an inner diameter of 4.5 cm and an outer diameter of 5 cm. The phantom is shown in Figure 4.9.

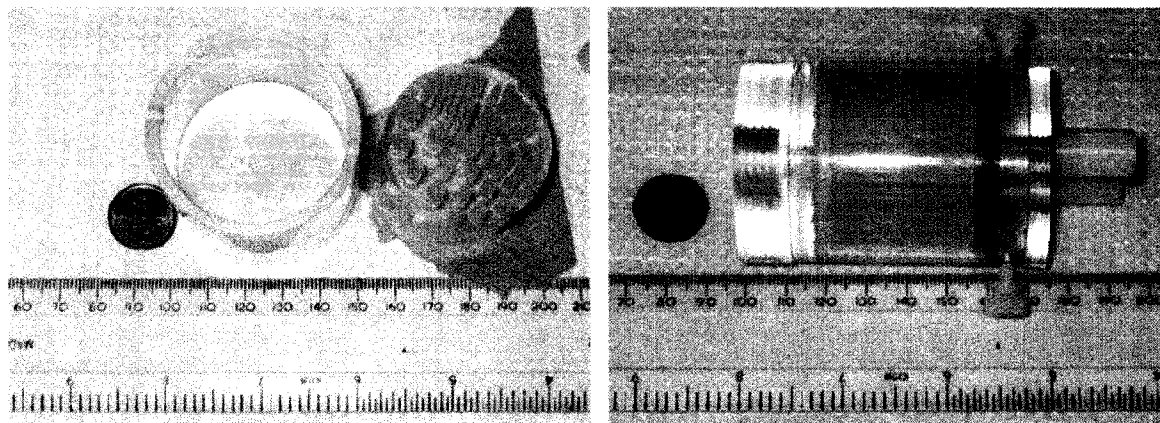


Figure 4.9. The Micro Deluxe Phantom™ with a hot rods insert.

Two experiments were performed employing the RS acquisition mode and the DS acquisition mode with the phantom aligned axially and centered in the transverse FOV. In both cases, an ^{18}F solution was injected into the phantom and data were acquired for one hour with 52 and 45 MBq of activity at the beginning of acquisition for the RS and

DS modes of operation. The images were reconstructed using MLEM with variable iterations (10, 50, 100, 200, 300, 400, 500, 600, 1000). Three different reconstructions were executed with the data and are summarized in Table 4.3. The central transverse image from each reconstruction was analyzed and the total counts in each central image are also shown in the table.

Table 4.3. Reconstructions performed to assess the resolution of the scanner

Reconstruction	Span	Counts (million)
Regular Sampling	3	0.68
Double Sampling	3	0.58
Regular Sampling	31	6.6

The final images obtained were 120 x 120 pixels with a 0.5 mm pixel spacing.

An example reconstructed image using MLEM with 50 iterations is shown in Figure 4.10 for the double sampling experiment.

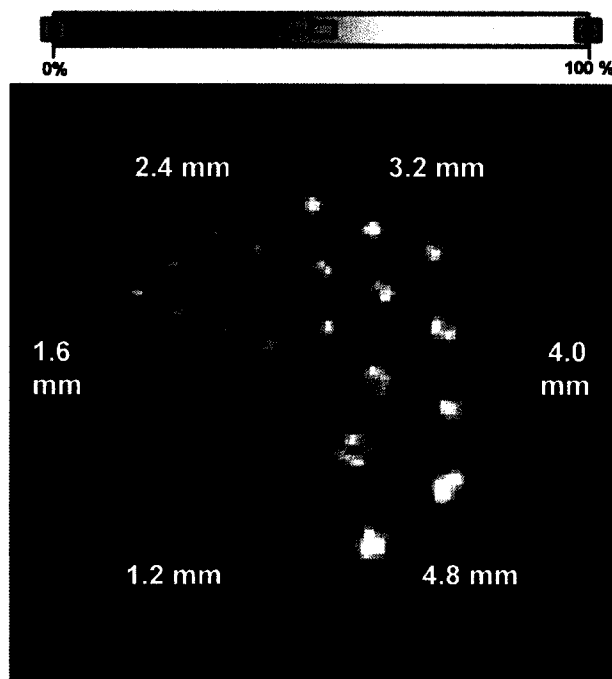


Figure 4.10. Reconstructed image of the Micro Deluxe Phantom™ for the double sampling acquisition mode using MLEM with 50 iterations. The dimensions noted are the diameters of the holes.

As is evident from the figure, the transaxial resolution lies between 1.6 – 2.4 mm, encouraging the creation of an algorithm to find the true image resolution between these values.

Evaluation of the resolution was then achieved by comparing peak recovery values for the hot spots in the reconstructed images to a computer simulation. The theoretical model employed in the computer simulation was a 2D Gaussian convolved with circular images, where the circles represent the phantom holes having the same dimensions. The following operation was performed:

$$f(x, y) ** g(x, y) = \frac{1}{2\pi\sigma_x\sigma_y} \int_{-\infty}^{\infty} \int_{-\infty}^{\infty} e^{-\left(\frac{x'^2}{2\sigma_x^2} + \frac{y'^2}{2\sigma_y^2}\right)} g(x - x', y - y') dx' dy' \quad (4.14)$$

where $f(x,y)$ is a 2D Gaussian and $g(x,y)$ is an image given by an NxN matrix. The Gaussian was assumed to be symmetric ($\sigma_x = \sigma_y$) and it acts as a model to the response function of the scanner. The images used for convolution are shown at the top of Figure 4.11. Profiles were then taken across the center of the simulated images before and after convolution to demonstrate the effect of the operation and this is shown on the bottom of the figure. The simulation was executed on a 1200 x 1200 pixel map, then downsampled to 120 x 120 pixels to simulate the reconstructed images from the scanner. The images shown are for a FWHM of 1.3 mm ($\sigma = 11$ pixels in simulation). The peaks (holes) are labelled 1-6 for referencing.

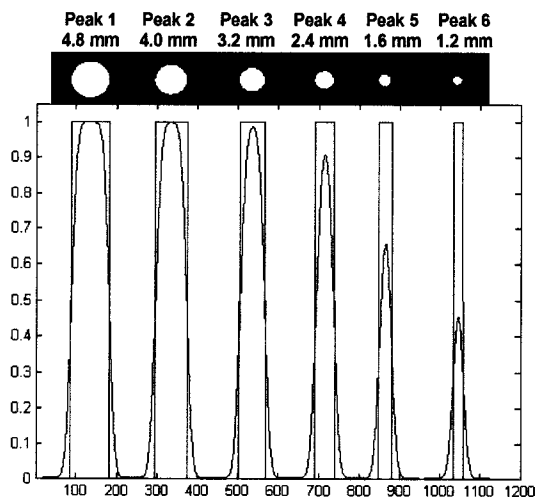


Figure 4.11. The images used for convolution in the computer simulation (top) with central profiles (bottom) of the images before (red) and after (blue) convolution with a FWHM = 1.3 mm.

The accuracy of the numerical simulation was verified by comparing peak values from the computer simulation to an analytical calculation for the case when the FWHM was equal to half of the hole diameter. The analytical calculation, shown in equation 4.15, was carried out by convolving a 2D Gaussian function in cylindrical coordinates (FWHM = $1/2$) to a circle of radius one, and evaluating the peak value. The simulation was then verified by changing the standard deviation of the Gaussian kernel in the simulation to correspond to the FWHM value that was half of the hole size width for each hole. The values are summarized in Table 4.4. The verification was done with only 1200 pixels to ensure accuracy.

Table 4.4. Simulated peak recovery ratios for holes of different sizes (FWHM = half of the hole diameter)

Hole size (mm)	FWHM for 1200 pixels	Peak Recovery Ratio
1.2	12	0.940
1.6	16	0.940
2.4	24	0.938
3.2	32	0.938
4.0	40	0.937
4.8	48	0.939

$$f(\rho, \phi) ** g(\rho, \phi) = \frac{1}{2\pi\sigma^2} \int_0^{2\pi} d\phi' \int_0^1 e^{-\left(\frac{\rho-\rho'}{\sqrt{2}\sigma}\right)^2} \rho' d\rho' \Big|_{\rho=0} = 0.938 \quad (4.15)$$

Comparing the values, it is observed that the numerical simulations are representative of the expected value of 0.938 and they were therefore concluded to be operating correctly.

For each central transverse image the peak value was recorded for each hot spot, and then averaged over all holes of the same diameter to obtain a single value. The ratio between successive peaks for both experimental and simulation data were then calculated (ie. 5/4, 4/3, 3/2 and 2/1). The ratios were then summed for the experimental and simulated data, and the difference was computed between the two sums. Hole 6 was not used in the computation because it was difficult to localize the peaks, as can be seen in Figure 4.10. The standard deviation of the Gaussian kernel was then adjusted until a minimum difference between the summed ratios was obtained. This standard deviation was then used to calculate the FWHM, where:

$$FWHM = 2.355\sigma \quad (4.16)$$

and this quantity was designated as the resolution of the image.

The transaxial resolution was found to have values bounded by 1.18 and 2.36 mm depending on the number of iterations and the acquisition/reconstruction mode used with the near optimal resolution occurring between 200 and 300 iterations. The results for all images are summarized in Figure 4.12, where the resolution is observed as a function of iterations.

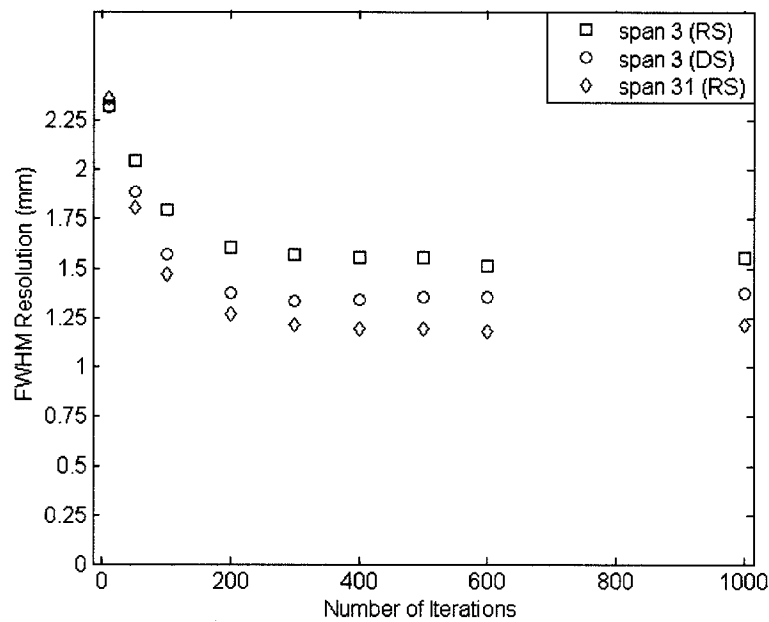


Figure 4.12. Reconstructed image resolution of MLEM versus the number of iterations for (a) regular sampling, span 3 (b) double sampling, span 3 and (c) regular sampling, span 31.

It was noticed that the resolution measured with double sampling and a span of 3 surpasses the regular sampling with a span of 3. This was due to the increased LOR density resulting from the additional sampling provided from the offset detector rings. Furthermore, the regular sampling with a span of 31 was found to outperform both of the other experiments. Here more of the LORs originating from the offset detectors were exploited leading to an even more finely sampled grid than with a double sampling acquisition. The result was an improved resolution that converged to 1.2 mm at a higher number of iterations which approaches the Nyquist limit for a 2 mm detector pitch. A span of 31 was thus adopted for any studies that are performed on the LabPET4™ scanner. Not only does it offer an improved resolution, but no bed motion is necessary and improved data statistics are obtained because all of the 3D counts are utilized. At the time of this evaluation only 0.5 mm pixels were available. With 0.25 mm pixels in the

reconstructed image, the more finely sampled LORs may be expected to have more accurate positioning leading to improved resolution. This should be investigated in future studies.

The MLEM reconstructed resolution demonstrates the high resolution necessary for cardiac imaging in small animals. A rat cardiac phantom was constructed to confirm this assertion. The phantom was based on quantities found in literature [35-38] and from measurements taken during a rat dissection. The end result was a phantom that represents an average sized rat with a left ventricle (LV), lung and liver cavity. The phantom was constructed of plastic with an attenuation coefficient very similar to that of soft tissue. The complete design including all dimensions is discussed in Appendix A. The notable dimensions are the width of the myocardium wall and cavity which were 3 mm and 6 mm respectively. A 5 minute regular sampling acquisition was completed with 75 MBq of an ^{18}F solution injected and the LV cavity centered in the axial and transverse FOVs. MLEM reconstruction was done with 20 iterations and a span of 31. An example transverse image is shown in Figure 4.13(a). A profile across the reconstructed image is also shown below. The blue dashed line on the reconstructed image indicates the location of the profile.

The peaks of the profiles were clearly resolved supporting the claim that the camera has the necessary resolution for cardiac imaging in rats. The measured distance between the maximum intensity peaks was 9 mm, which was supported from the rat phantom diagram as this was the distance between the middle of one wall to the middle of the other wall. Furthermore, a simulation was completed where an annulus was drawn representing the LV myocardial wall in the phantom, with the same dimension, and then

Gaussian smoothing with a FWHM of 2.2 mm was applied to simulate the response function of the scanner and the expected resolution at ~ 20 iterations. This is illustrated in Figure 4.13(b). The image of the cavity is shown at the top, prior to applying the response function. The blue line below is a profile before smoothing and its location is depicted by the blue dashed line above. The red line in the profile shows the effect of the response function on the data.

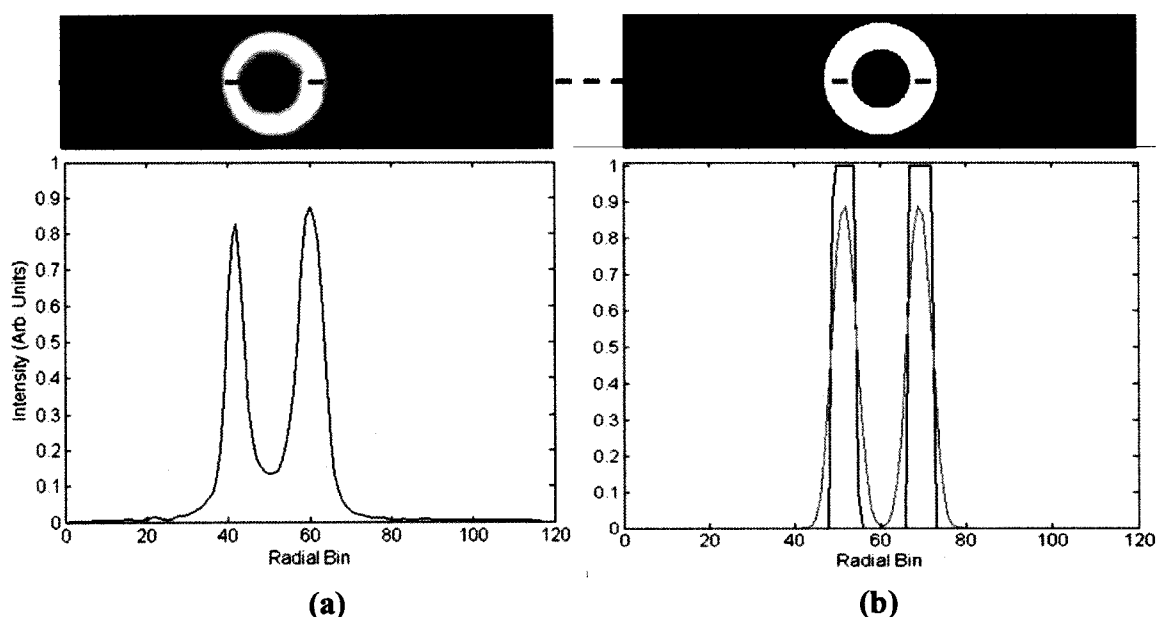


Figure 4.13. Transverse images of the rat phantom with lines drawn across (top) to illustrate the profiles shown below (bottom): (a) the rat phantom from experimental data; (b) a simulated rat phantom before applying the response function (top) with a profile before (blue) and after (red) the Gaussian (FWHM = 2.2 mm) response function has been applied.

The peak-to-peak distance was again measured to be 9.0 mm in this case. The purpose of this simulation was to demonstrate the necessary resolution and to explore the accuracy of the assumption that the system response model function is Gaussian. The behaviour was similar for the experiment and the simulation. The relative peak value recorded from the profile of the reconstructed image was 87%, while the peak value from the simulation was 88%, confirming the accuracy of the assumption that the system

response model is Gaussian. However, there are still some differences in the shapes of the profiles. A broadening in the distribution of the profiles across the reconstructed image was noted, with residual activity recorded between the walls of the active regions. Furthermore, there was also activity located outside of the object. This may be due to scatter and will be a topic for discussion in a following section.

To further confirm the phantom results, a live rat was imaged along with a live mouse with an ^{18}F -FDG tracer. 21 MBq was injected in the mouse and it was imaged for 15 minutes 30 minutes after injection. 120 MBq was injected in the rat and was imaged for 5 minutes, 15 minutes following the injection. The images are shown in Figure 4.14.

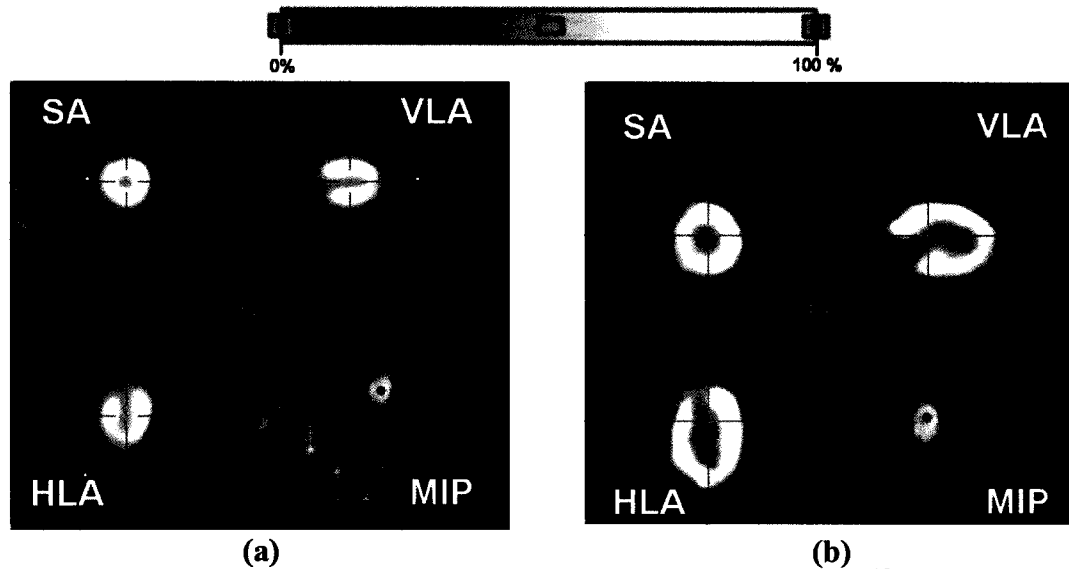


Figure 4.14. Cardiac images of the LV in a mouse and rat using ^{18}F -FDG and 15 MLEM iterations with a span of 31. SA is the short axis view, VLA is the vertical long axis, HLA is the horizontal long axis and MIP is the maximum intensity projection through all slices. (a) A 15 minute LV image of a healthy mouse 30 minutes after an intraperitoneal injection (abdominal lining) of 21 MBq of activity. (b) A 5 minute LV image of a healthy rat 15 minutes after an intravenous injection of 120 MBq of activity.

The rat and mouse LV cavity of the heart is clearly resolved in both cases leading to the conclusion that the number of counts and resolution are sufficient for cardiac uptake imaging in these animals. In the live mouse image presented, the distance

between the peaks of the myocardium was 3.8 mm, thus the camera has the resolving power to discriminate between the walls of the LV in mice. Furthermore, the distance between the peaks of the myocardial walls was found to be 8.5 mm in the live rat study, which was comparable to the 9 mm measured with the rat LV phantom, supporting the accuracy of the design of the LV cavity in the phantom. The scanner thus demonstrates the necessary resolution and count rate capability to resolve the myocardium with static FDG uptake imaging in rats and mice.

4.6. Image Non-Uniformity

Image non-uniformity is a measurement for a uniform activity distribution that gives insight into the accuracy of the normalization correction applied to the data. It is also a useful tool for assessing scatter and attenuation correction. It is defined as the variability of the data in terms of the sample standard deviation (s) and the mean value (\bar{x}):

$$\text{non - uniformity} = \frac{s}{\bar{x}} \quad (4.17)$$

For this experiment, a uniform flood phantom with a 6 cm diameter that provides a homogeneous activity region throughout the FOV was chosen. The phantom was filled with 93 MBq of an ^{18}F solution and data were acquired for 3 hours to avoid counting statistics limitations. The images were reconstructed with MLEM using 20 iterations and a span of 31 to incorporate all 3D counts. MLEM was used here because it was adopted as the reconstruction standard for animal studies. The reconstructed images were then imported into MATLAB for further analysis. The central transverse image is shown in Figure 4.15. A region of interest was defined on each transverse plane encompassing the

central 75% of the phantom (4.5 cm) in diameter which is illustrated below. The mean intensity was calculated for each plane, accompanied by the maximum and minimum intensity, and all three quantities were plotted versus plane number as depicted in Figure 4.16.

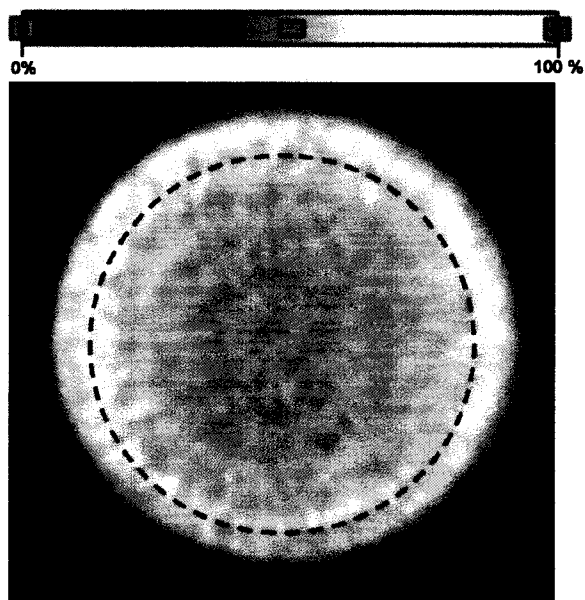


Figure 4.15. Central transverse image of the uniform flood phantom (plane 17) with the circular region of interest depicted by the dashed line.

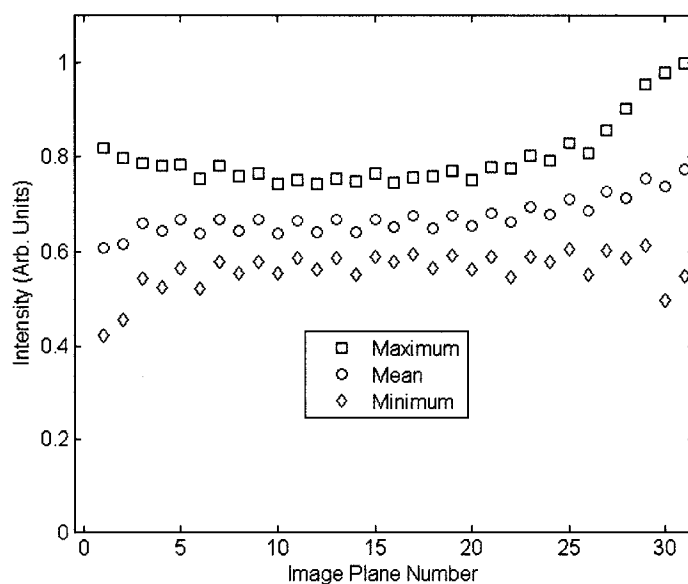


Figure 4.16. Plot of the maximum, mean and minimum values from the region of interest drawn on the uniformity phantom versus the image plane number to demonstrate the variability of the data.

This figure enables a visual assessment of the variability of the recorded data. It was noted that towards the end planes there are larger variations in the data. This was a result of lower counting statistics from the data due to the maximum allotted span. The maximum ring difference in the central plane was 15, while at the end planes it was zero. Therefore, only direct planes contribute to the counts in the end planes, thus reducing the counting statistics, while in the central region there are 31 planes contributing with a corresponding span of 31. These data suggest that subjects should be placed towards the central region inside the scanner for optimal image uniformity. Secondly, the standard deviation and the mean value were found over all planes within the region of interest. The recorded image non-uniformity was then calculated over all planes and found to be 9.2%. In general, the acceptable standard is to record an image non-uniformity less than 10% over all planes. The measured value falls below the acceptable standard, therefore, it was concluded that the normalization correction available on the LabPET4™ scanner is sufficiently accurate.

4.7. Assessment of Attenuation and Scatter

With any imaging system, image quality can be degraded due to measurement or reconstruction artifacts. The main sources of artifacts in PET are generally attributed to detector and geometric efficiencies, dead time, and photon attenuation and scatter. Normalization has been shown to correct for the efficiencies on the LabPET4™ as discussed, and a dead time correction has been shown to be necessary for accurate measurements at or beyond the peak NEC. The other sources of artifacts, in the form of attenuation and scatter, also play a role in degrading image quality and are thus discussed here in more detail. The first topic to consider is photon attenuation. As mentioned in

Chapter 1, photon attenuation occurs when either one or both of the annihilation photons is absorbed or scattered in the medium and goes undetected. An example of this can be seen in Figure 4.15. The reconstructed count rate is lower towards the center of the object as a brighter region is observed near the outside of the object, neglecting the red ring around the object which is believed to originate from scatter. To fully envision this phenomenon a profile through the center of the object is shown in Figure 4.17.

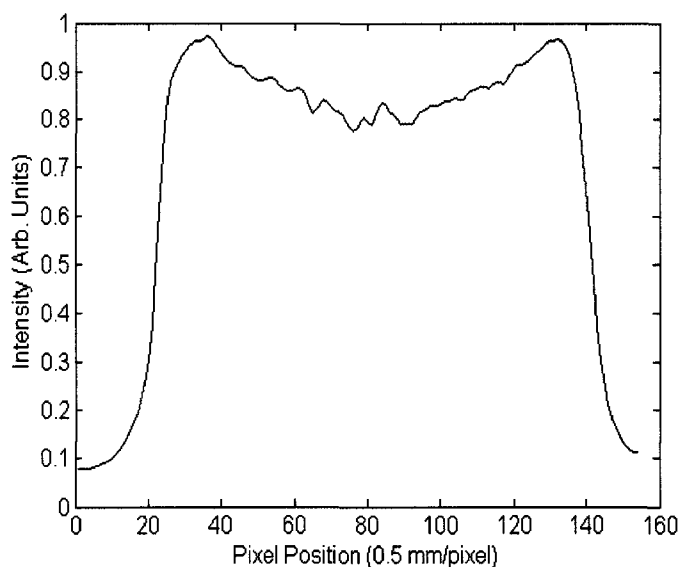


Figure 4.17. Profile across the uniformity phantom from Figure 4.15 to demonstrate the effect of photon attenuation.

Figure 4.17 reveals a cupping artifact suggesting photons are absorbed with absorption being favoured towards the central portion of the object. Upon comparing the minimum intensity in the object center to the maximum intensity, it is found that at least 20% of the photons that originate from the object center are absorbed relative to the edges. Taking only narrow beam attenuation across a 6 cm uniform cylinder into consideration, it is expected that 44% of the photons will be attenuated at the object center, assuming the phantom is positioned in the center of the FOV. The difference between the measured absorption and predicted attenuation are partly due to recorded

scatter events which have an affinity for the object center. Furthermore, the edges of the object are not well defined because the LORs which define the edges of the cylinder still intersect the object and are thus subject to attenuation. There is also a broad distribution outside of the object which is due to scattered events being recorded. The LORs are thus mispositioned and this is why a red ring is observed around the object in Figure 4.15.

Thus, from examination of the uniform phantom it is noticed that scatter and attenuation are non-negligible, and it demonstrates that these corrections are necessary. The predicted 44% photon attenuation suggests that this correction is absolutely necessary when dealing with objects on the order of the size of the flood phantom. The 6 cm diameter is only slightly larger than the average sized rat, which was found to be 5.4 cm when constructing the rat phantom. Furthermore, the indented profile leads to degradation in image uniformity because of the higher variability presented from the profile.

To assess the magnitude of scatter, the rat LV phantom was studied. Figure 4.13(b) shows that the profile across the simulated LV cavity should fall to zero between the active regions and the profile had a well defined shape. Upon comparing this to Figure 4.13(a), it was noticed that there remained activity in between the walls. This was a direct result of mispositioned LORs due to photon scatter, as discussed in Chapter 1. Furthermore, outside of the cavity there was a broadening of the profile, which can also be attributed to photons scattering within the phantom and the detection system. The ratio between the minimum value observed between the cavities to the maximum peak recorded was 15% suggesting that the scatter contribution was not negligible. Furthermore, the scatter fractions measured in section 4.3 were 22 and 28% for the

mouse-like and rat-like phantoms respectively. Finally, it was noted that inside the cavities of the live rat and mouse study, shown in Figure 4.14, that there still remained activity which can be attributed partly to scattered photons being recorded. These results support the fact that scatter correction in objects on the order of these sizes must be considered for this system. Scatter correction will be regarded in more detail in the following chapter.

4.8. System Comparison

To put the performance measures of the LabPET4™ system into perspective it is compared to other cameras currently available on the commercial market. Two other small animal PET cameras available include the microPET® - FOCUS-F120 (CTI-Concorde Microsystems LLC, Knoxville, TN) and the quad-HIDAC (Oxford Positron Systems, Weston-on-the-Green, UK). The microPET®-F120 is a PMT based scanner with position sensitive PMTs and Lutetium oxyorthosilicate (LSO) scintillator crystals. It has a 14.7 cm transverse FOV and extends 7.6 cm axially. The quad-HIDAC is a scanner based on high-density avalanche chamber detector modules constructed from argon filled MWPCs. The camera has a 17 cm diameter with a 28 cm axial extent. Recent performance evaluations of these systems are accessible [39;40] and the following discussion is based on these references and the work provided in this chapter.

The peak sensitivity of the microPET®- F120 camera at the center of the axial and transverse FOVs was measured to be 7.1% following the animal PET scanner standard with an average of 3.5% across the FOV. The sensitivity of the quad-HIDAC was measured with a 6.1 cm line source with a 0.8 mm diameter active region. The average sensitivity of the line source was measured at 1.2%. In both cases the sensitivity was

superior to the LabPET4™ which had a peak sensitivity of 0.6%. The large improvement of the microPET®-F120 sensitivity is predicted to yield a higher SNR occurring at a lower activity in comparison to the LabPET4™. The enhanced sensitivity of the microPET®- F120 is due to an increased axial FOV and a higher packing fraction because blocks of detectors are used rather than individual crystals. The improved sensitivity recorded for the quad-HIDAC can be attributed to the large axial FOV of the camera. A second version of the present scanner is available, known as the LabPET8™. This has twice the axial FOV, thus an improvement in sensitivity to 1.2% is expected [41].

The scatter fraction of the microPET®-F120 was determined in the same manner as discussed in section 4.3. The values for the mouse and rat-like phantoms were 12% and 26% respectively with a 250 keV lower energy threshold showing an improvement in comparison to the values of 22% and 28% respectively for the LabPET4™ scanner. The differences observed can be attributed to the scanner geometry and the fact that the microPET®-F120 better discriminates against Compton interactions. It is believed that the LabPET4™ system may introduce additional scatter from the gantry and detectors which is why the values are not equal. Furthermore, the quad-HIDAC measures the scatter fraction by fitting an exponential tail outside of the discussed line source in air and in a mouse-like phantom which is a uniform phantom with a 6.2 mm length and 26 mm diameter. The scatter fractions of these studies were recorded as 23% and 29% with a 200 keV window. The line source measurements in air suggest that most of the scatter in these measurements originates from within the gantry and detectors. By introducing a mouse-like phantom, the scatter fraction only changes by 6%. This has led to the idea

that the different end shield inserts available on the LabPET4™ must be tested and different sizes evaluated to see how this changes the scatter fraction and to further observe the impact on the NEC. It was possible that the end shield insert may have had a negative effect on the scatter fraction and this should be tested in future studies.

The peak NEC as measured by the microPET®-F120 with a 6 ns timing window and a 250 keV lower level discriminator gives 809 kcps at 88 MBq of activity and 300 kcps at 150 MBq of activity for the mouse-like and rat-like phantoms respectively. These were measured in a similar fashion to those presented in section 4.3. The results are again superior to the 42.0 kcps at 110 MBq and the 13.7 kcps at 156 MBq for the mouse and rat-like phantoms that were recorded for the LabPET4™ system. The increased NEC in the microPET®-F120 can be attributed to the following: increased sensitivity, a smaller allowed timing window of 6 ns compared to 20 ns for the LabPET™ so more randoms are rejected, and the fact that the randoms are corrected from singles so the factor a is of unity in equation 4.6. This confirms that improvements are necessary in sensitivity, timing resolution, and randoms correction to produce a higher peak NEC on the LabPET4™. An NEC measurement was not obtained for the quad-HIDAC, however the peak prompt count rate for the line source in air was recorded to be 220 kcps and the randoms rate was recorded to be ~90kcps, both at 16 MBq. The peak prompt count rate on the LabPET4™ was 280 kcps at 300 MBq in the rat-like phantom suggesting dead time was not as limiting as on the quad-HIDAC. On the quad-HIDAC, the randoms are corrected from single events, thus using the measured 23% scatter fraction a rough NEC calculation could be obtained using equation 4.6. This was found to give 45 kcps, which was roughly comparable to the rate measured in the mouse-like phantom with the

LabPET4™. This could not be directly compared because this measurement was taken from a line source measurement in air and was not necessarily the peak NEC, thus this calculation only provides an estimate. Furthermore, this measurement was done in air, thus a lower peak NEC would be recorded if the mouse-like phantom was used. Therefore, it is predicted that the LabPET4™ should have a higher peak NEC than the quad-HIDAC.

The LabPET4™ system was shown to obtain a 1.2 mm resolution in section 4.5 using a high number of MLEM iterations while the FBP resolution was measured to be 1.7 mm at 5 mm off center [41]. The microPET®-F120 system had a resolution of 1.8 mm at 5 mm of center using FBP, and the quad-HIDAC demonstrated a 1-1.1 mm resolution at the center of the FOV using one pass list mode expectation maximization (OPLEM) and FBP. It was also shown that transverse resolution at 20 mm off center was 1.2 mm with FBP. The quad-HIDAC thus shows superior resolution in comparison to the two other systems. The microPET®-F120 system had a very similar FBP resolution in comparison to the LabPET4™, so it is predicted that a similar resolution would be obtained with an iterative reconstruction. However, the peak NEC rate is higher on the microPET®-F120 which would enable it to obtain a higher reconstructed resolution in animal studies when count rates are limited. A higher number of iterations could be used in comparison to the LabPET4™ system because the noise amplification introduced by MLEM reconstruction would occur at a later number of iterations, thus enabling the microPET®-F120 system to achieve a higher resolution. The performance parameters discussed thus far are summarized in Table 4.5 for each of the systems.

Table 4.5. Comparison of the performance parameters of the LabPET4™ to the microPET®-F120 and the quad-HIDAC

	LabPET4™	microPET®-F120	quad-HIDAC
Sensitivity	0.6% (peak)	7.1% (peak)	1.2% (average)
Peak NEC (mouse-like phantom)	42 kcps at 110 MBq	809 kcps at 88 MBq	45 kcps at 16 MBq (estimated)
Scatter Fraction (mouse-like phantom)	22%	12%	29%
Resolution	1.7 mm (FBP) at 5 mm off center 1.2 mm (MLEM)	1.8 mm (FBP) at 5 mm off center	1-1.1 mm (FBP,OPLEM) at center

The microPET®-F120 system had a dead time of 50% at 152 MBq in the rat-like phantom which is half the corresponding activity recorded for the LabPET4™ camera. The LabPET4™ camera is thus able to acquire images with higher activities in the FOV without significant dead time losses. Furthermore, the non-uniformity of a 6 cm uniform phantom was measured with a value of 4% in the central 2.4 cm of the scanner with scatter and attenuation corrections applied, as compared to the LabPET4™ which has 9.2% non-uniformity over all planes without any corrections. The non-uniformity calculation was adjusted to only include the central 2.4 cm of the LabPET4™ scanner's axial FOV and this calculation yielded 7.3%. Although these values cannot be directly compared they support the need for scatter and attenuation algorithms to be implemented on the LabPET4™ scanner.

In conclusion, although the LabPET4™ system has been shown to have the capability for static cardiac uptake imaging in small animals, other commercial scanners have the ability to perform the same tasks with higher resolution or shorter scan times. The LabPET4™ has a better count rate performance than the quad-HIDAC however, the

quad-HIDAC had a better resolution performance. In the case of the microPET® -F120 system, the performance measures are superior to the LabPET4™ camera. Many improvements would need to be addressed and implemented on the LabPET4™ camera to obtain similar performance parameters as the microPET®-F120.

Chapter 5 –Attenuation and Scatter Correction

5.1. Introduction

If one of the annihilation photons originating from the activity inside an object interacts in the medium, photon attenuation will occur. If the photon changes direction and its residual energy remains within the given energy window it may still be recorded in a different LOR, which is referred to as scatter. Attenuation and scatter correction is a popular topic in PET imaging because both effects degrade image quality. Techniques to correct for both phenomena have been explored in detail and many algorithms have been developed to overcome the limitations posed on image quality. Although in soft tissue the main contribution to the attenuation coefficient is Compton scatter, PET systems have sufficient energy resolution to reject some scattered photons so that large angle scatter can go undetected. In contrast, scattered photons that occur above the energy threshold will be recorded and thus deteriorate image quality because the events will be mispositioned. In the ideal system, the width of the energy window would be very small (ie. 1 keV), and would reject all Compton scattered photons. However, PET systems have a finite energy resolution. For example, the LabPET™ system has an average energy resolution of 23% and 28% for the LYSO and LGSO detectors respectively [41]. Consequently, the energy window must be broadened to ensure that a minimal amount of true counts are lost. As a result, scatter will appear and must be corrected for. This section will address phantom studies to observe the effectiveness of scatter and

attenuation correction to gain insight into whether these algorithms will help improve image quality in rat and mouse studies.

5.2. Attenuation Correction

Attenuation correction is typically obtained through calculation of the ACFs, as discussed in Chapter 3 and defined by equation 3.1. The most common method is to use an external positron emitting source, such as ^{68}Ge , to measure the transmission data using coincidence detection. The ACFs are smoothed and then applied to the emission data through multiplication prior to image reconstruction. A smoothed version is used so that local variations in the ACF measurements do not introduce noise into the emission data. Methods that use transmission scanning to find the ACFs are referred to as direct measurements because they do not make any assumptions of object shape or of the attenuation coefficient distribution [5]. The limitation of using transmission imaging is that sufficient counts must be acquired to obtain a suitable estimate of the ACFs [5]. Since it is not always possible to obtain sufficient counts, a method using a low count transmission scan was proposed by Meikle *et al.* [9] in order to find the ACFs. The transmission scan was first reconstructed, and then segmented into predefined regions, namely air, lung and soft tissue. The linear attenuation coefficients were assigned to each of the corresponding regions. The image was then forward projected to obtain the ACFs in sinogram space so they could be applied to emission data.

Singles events may also be used for transmission measurement. This can be obtained with a positron emission source [10], or using a single photon emitter such as ^{137}Cs [11;12]. In the method described by deKemp and Nahmias [10], a ^{68}Ge rotating rod source was used and transmission data were acquired by rotating the rod source while

only acquiring single events on the opposite side to where the source was located.

Knowing the source location, the LOR of the singles counts could be identified. A blank scan was obtained in a similar manner and the ACFs were calculated. Other singles transmission measurements were obtained using a scanning point source of ^{137}Cs [11;12]. An extrapolation algorithm was used to convert attenuation coefficients at 662 keV (E_γ for ^{137}Cs) to 511 keV in [11]. In [12] the transmission images were first reconstructed and segmented. Known attenuation coefficient values for 511 keV were then inserted into these compartments. Recent scanners are beginning to adopt a CT component located beside the PET camera to perform rapid attenuation correction. An estimate of the ACFs is obtained by scaling the values measured with CT to 511 keV so they can be used to correct PET emission data [42].

Although the measured attenuation correction through transmission scanning is more accurate, because it is a direct measurement of the attenuation distribution [5], attenuation correction may be estimated directly from emission data. A calculated attenuation method was proposed by Bergstrom *et al.* [7], which was later refined by Siegel and Dahlbom [8]. Bergstrom *et al.* [7] used a contour finding algorithm in projection space and backprojected these contours to give 19 points around the object in image space. Chord lengths were then drawn in image space using the defined points to determine the attenuation length. Siegel and Dahlbom [8] modified the algorithm to produce a continuous contour in image space rather than assigning discrete points.

To fully appreciate the effect of attenuation correction on an object, the uniformity phantom discussed in section 4.6 was examined to see if attenuation correction could partially restore the image uniformity. It was shown in the profile of

Figure 4.17 that the central region of the phantom, illustrated in Figure 4.15, suffered from photon losses due to attenuation. To correct for attenuation in this phantom, transmission imaging was utilized from the QA measurement described in Chapter 3. Transmission scanning was employed because it should provide an accurate estimate of the ACFs as discussed and it is hoped to be adopted as the standard for attenuation correction on the LabPET4™ scanner. To perform this task, the 250 mL phantom was filled with water and placed on the bed. Blank and transmission scans were obtained and the ACFs were calculated following the same methodology provided in Chapter 3. The phantom was then filled with 90 MBq of an ^{18}F solution and an emission scan was acquired for three hours in the same position as the transmission scan to conserve positioning of the phantom in both the transmission and emission scans so the two could be directly overlaid during ACF multiplication.

Sinograms were then constructed for the three different scans obtained. In all cases a span of 31 was used and the emission sinogram was normalized using the blank scan obtained. The ACFs were then calculated and multiplied by the emission data to obtain an attenuation corrected sinogram. The blank and transmission sinograms were smoothed with a Gaussian filter having a standard deviation of 2.5 mm in the radial direction and 3.8° in the angular direction. The filter was cutoff beyond 11.3° in the angular direction and 7.5 mm in the radial direction. The characteristics of the filter were chosen based on multiple measurements. Filters of different standard deviations were compared until a suitable non-uniformity was found and changing the standard deviation by 0.5 mm and 0.75° did not change the image non-uniformity by more than 0.1%. The filter was used to ensure there was no division by zero when calculating the ratio and so

additional noise introduced into the emission data by multiplication of the ACFs was minimal. Both the uncorrected and corrected sinograms were then reconstructed using FBP. This reconstruction method was used because MLEM sinogram reconstruction was not available on the LabPET4™ scanner. The image non-uniformity was then evaluated for both cases for the middle 75% (4.5 cm) of the phantom in the central transverse plane. The non-uniformities were found to be 9.9% before correction and 8.3% after correction. It was therefore observed that the uniformity was improved by 1.6% with attenuation correction obtained through transmission scanning. To visually see the increased image quality, the central images for the corrected and uncorrected data are shown in Figure 5.1. A profile was also taken across the image to visually confirm the increased uniformity.

It was confirmed visually that there was in fact an improvement in non-uniformity as the image demonstrates an increased homogeneity after the attenuation correction has been applied. Additionally, the profile taken across the uncorrected image shows the indented profile as discussed in Section 4.7. The corrected profile was observed to have a flatter response, which is seen in Figure 5.1(b). The results support that attenuation correction has a positive effect on image non-uniformity, resulting in better image quality and a flatter response across the image. Transmission imaging was therefore concluded to be a possible consideration on the LabPET4™ scanner.

Scatter was present in both the transmission and emission scans and can be noticed in the tails of the profile because they are not sharp, but seem to form a continuum. Scatter will alter contrast and introduce additional noise in the image, thus, the next section will address scatter correction to study the effectiveness of correcting for this phenomenon.

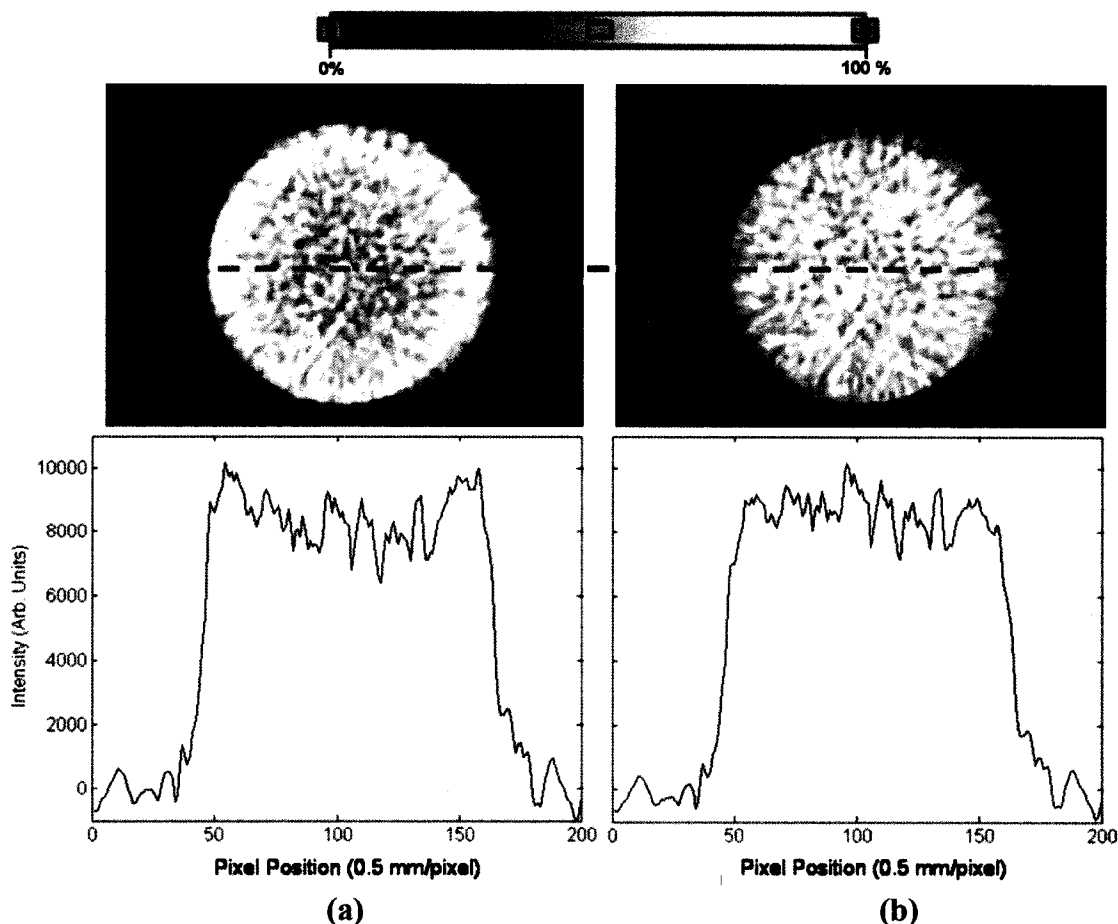


Figure 5.1. Central transverse images of (a) non-corrected and (b) attenuation corrected data for the 250 mL Nalgene bottle (top). The blue line drawn across the images depicts the location of the profiles shown on the bottom of the image. The profile on the right is shown to have the indented profile removed as a result of photon attenuation being corrected.

5.3. Scatter Correction

Scatter correction has been discussed in much detail and a variety of algorithms have been proposed to address this problem. These consist of simulations to calculate scatter distribution, energy window manipulations, incorporation of scatter correction algorithms directly into the reconstruction process, the use of collimation, and analytical approaches estimated from projection or image data. Simulation based approaches include methods proposed by Levin, *et al.* [19], Ollinger [18], and Watson, *et al.* [17].

The technique delineated by Levin *et al.* [19] simulated the scatter component using the emission image as a starting point to the true source distribution. The image was then input into a Monte Carlo simulation that incorporates the scanner's true geometry. The algorithm then traced the history of the photons and their interactions in the scattering medium. The scatter distribution was then sorted into its respective sinogram. The measurement of the true component was then computed by the difference between the measured data and the scattered component. Ollinger J.M. [18] used a transmission scan, an emission scan, the physics of Compton scattering and a mathematical model of the scanner to calculate the number of photons that underwent a single scatter. The single scatter distribution was used to further model multiple scattering. The method outlined in [17] works in a similar manner. 2-D estimates of the emission and attenuation distributions were initially obtained. The single scatter distribution was estimated for points in projection space by calculating a volume integral over the scattering medium with a scattering kernel derived from the emission image, attenuation coefficients, photon energies before and after scattering, and the scattering angle. The calculated scatter distribution was then subtracted from the emission image. Despite their accuracy, the model based approaches discussed do not account for scatter that occurs outside of the FOV of the scanner [17-19]; however, scaling to the scatter distribution tails outside of the object may account for some scatter outside of the FOV [18].

Another group of scatter correction algorithms rely on energy window manipulations to obtain information about the scatter distribution. One of these methods used a dual energy window [16] and an extension of this method was utilized to perform a multi-energy window scatter distribution estimate [22]. Grootoenk *et al.* [16] assigned

coincidence events to two energy windows occurring over the photopeak (380-850 keV) and over the Compton regime (200-380 keV). A fraction of the counts found in the lower energy window were then subtracted from the upper window. The fraction was derived from phantom measurements where line sources were placed in head-sized geometries and data were acquired in both energy windows. The scatter distribution was estimated by taking the difference between the upper and a fraction of the lower energy windows. The multi-energy window used a number of energy windows, each with the same width [22]. The spatial distribution of the scattered and unscattered components presented in each window was fitted to mono-exponential functions and then approximated with analytical functions. The functions were used to obtain position sensitive scatter kernels for each energy window. Unfortunately, the energy methods require prior knowledge of the object and therefore are only practical for well-defined geometries which do not vary between studies (eg. the adult brain) [5]. Energy information has also been directly integrated into the reconstruction procedure [21]. The energy information from list mode was used to discriminate between scattered and unscattered photons. The unscattered component was determined from detector measurements while the average scatter component was determined from measurements and simulations for typical phantom and patient sizes. This information was then incorporated directly into MLEM reconstruction.

A unique method proposed by Chuang, *et al.* [23] used a beam stopper device that was constructed from a high Z material. The device was placed in front of a detector to block true events from being recorded taking into consideration transmission through the material. The LORs that recorded counts at the intersection with the beam stopper are

said to have originated from scatter since true events were blocked. Multiple beam stoppers were used and an estimate of the scatter distribution was obtained utilizing the counts recorded in the blocked detectors.

Scatter correction may also be obtained using analytical functions. The common methods used for this include the integral transformation of projections [15], a convolution-subtraction algorithm [20], and fitting the scatter outside of the object to a smoothly varying function [13;14]. The integral transformation method described in [15] measured the scatter distributions of line sources which were placed in various locations inside scattering media of different dimensions. The projected distributions were then analytically expressed. The functions were subtracted from emission data, which were blurred due to these scatter components. Bailey, *et al.* [20] proposed to estimate the scatter distribution by convolving photopeak projections with a mono-exponential function, assuming that there exists a relationship between scatter and photopeak data. The projection data were corrected prior to reconstruction. Finally, the methods described in [13;14] used the fact that recorded counts originating from outside the active region must have been scattered. The tails located in projection space outside of the object were then fit to an analytic function (eg. a Gaussian), and then subtracted from the emission data to obtain the scatter corrected data. This method also had the advantage that it corrected for some scatter outside of the FOV.

To study the effect of scatter correction on image quality, a cold rod phantom was considered that had a hot (active) region and cold (non-active) regions. A drawing of the phantom used is shown in Figure 5.2. The phantom was constructed from acrylic; $\mu = 0.111 \text{ cm}^{-1}$ at 511 keV [43]. It had an outer diameter of 33.5 mm and an inner diameter

of 30 mm that could be filled with activity. The length of the outer region of the phantom was 36 mm while the inner length was 30 mm. The fillable cold regions had an inner diameter of 8 mm, with a 10 mm outer diameter, and were located at 1.25 mm from the walls of the phantom on either side. This particular phantom was used to evaluate scatter correction because it consisted of two cold regions that, in theory, should not show any recorded activity in the reconstructed images. If activity is recorded in these regions it can be assumed to originate from scattered events. Furthermore, the two cold regions allowed evaluation of the scatter contribution at different points inside the scanner.

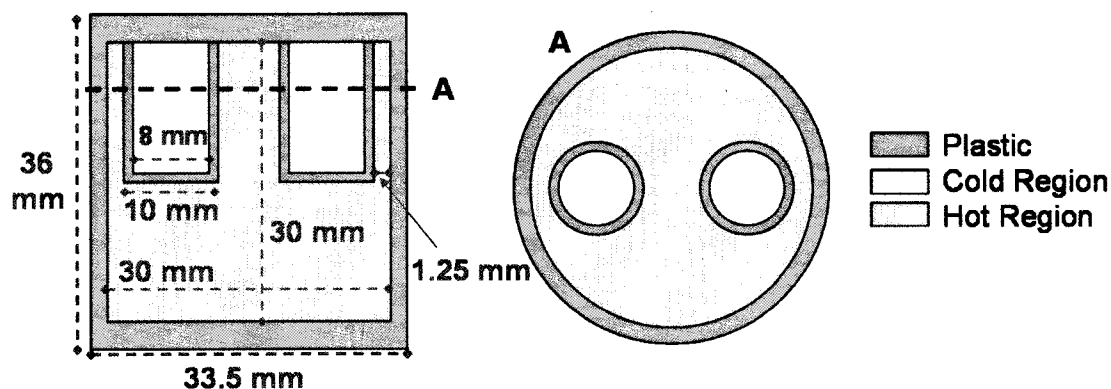


Figure 5.2. Illustration of the cold rod phantom used for scatter correction.

For this experiment, the hot region was filled with 75 MBq of an ^{18}F solution while the cold regions were filled with water. The phantom was scanned for 1 hour with the double sampling acquisition mode. The placement of the phantom was in the center of the transverse and axial FOVs. Sinograms were then constructed for each image plane with SSRB and a span of 31. The sinograms were normalized with a blank scan that was obtained with the daily QA and the random events were corrected using the available delayed window measurements. The emission sinogram recorded for the object was expected to have well defined edges. However, because of the energy window employed, scatter events were recorded producing a blurring of the edges outside of the object. The

distribution of the tails was then fitted to a Gaussian to estimate the scatter distribution of each angular projection in sinogram space [13;14]. This scatter correction algorithm was chosen because it helps correct for scatter outside the FOV and the calculation can be analytically executed in sinogram space without requiring any additional measurements or computer simulation.

The edges of the object were primarily estimated following an edge detection algorithm described by Siegel, *et al.* [8]. The sinogram profiles were first summed into 8 independent sections. A first derivative was then applied to each of the summed profiles and the pixels occurring at 20% of the maximum and minimum were found in order to obtain an initial estimate of the left and right edges of the sinogram respectively. Using the estimated edges and the midpoints occurring between them, the sinograms were partitioned into 16 (8 left and 8 right sides) activity regions (AR) providing an initial estimate of where the object was actually positioned. The data lying outside of this region were sectioned into 16 scatter background (SB) sections, having again 8 left pairs and 8 right pairs. The mean counts per pixel were calculated in each of the AR sections and the SB sections to obtain the mean activity uptake per pixel (MAU) and the mean scatter background per pixel (MSB), respectively. Thresholds were then defined as the average between MAU and MSB for each of the sections. All projections in each section of the sinograms were searched from the left and right to find their respective thresholds. The pixels occurring on these thresholds were defined as the edges of the sinogram.

The data occurring outside of the edges were then fitted to a Gaussian of the form:

$$f(x) = ae^{-\left(\frac{x-b}{c}\right)^2} \quad (5.1)$$

where a , b , and c are free variables determined by the fitting algorithm and x is the radial position. MATLAB was used to perform the fitting using the method of non-linear least squares. Once the Gaussian profile had been fitted to the data, it was subtracted from its respective emission profile. This was done for each projection in all of the sinograms to obtain scatter corrected sinograms. Example profiles, including an uncorrected emission projection, a fitted scatter profile and the scatter corrected profile, are shown for one projection in the sinogram in Figure 5.3.

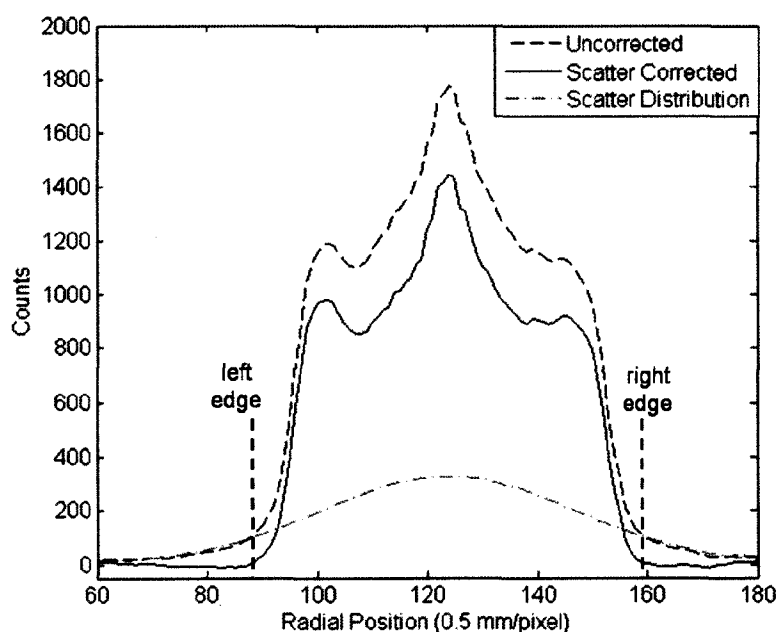


Figure 5.3. Profiles for a row in the sinogram to show the effect of scatter correction. The uncorrected projection is shown with the scatter corrected profile and the scatter distribution profile. The determined edges are also shown.

The effect of scatter correction on a profile was evident from the figure. The uncorrected data had a broader distribution outside of the object, whereas the scatter corrected data had much more abrupt edge definition. Furthermore, the overall counts were decreased; however, these counts were all assumed to originate from scatter. As a first check, the total counts in the uncorrected and scatter corrected data sets were

measured and the ratio of the scatter to the total counts was computed. The fraction of the total counts subtracted was 25%, which occurs between the 22% and 28% scatter fractions measured for the mouse-like and rat-like phantoms, as discussed in section 4.3. This was expected because the phantom considered for scatter correction had a diameter that was between the mouse and rat-like phantoms. Although the measured scatter fractions are comparable, they cannot be directly associated because the activity distributions are not identical. This calculation could, therefore, only be used as a preliminary check to suggest that the scatter correction algorithm was operating correctly.

To fully demonstrate the effectiveness of the fitting technique, the original emission sinograms and the scatter corrected sinograms were reconstructed with FBP. Regions of interest (ROIs) were then drawn in the cold and hot regions as illustrated on the reconstructed image in Figure 5.4. Each region had a circular diameter of 5.5 mm and encompassed 10.7 cm axially, ie. the axial extent of the cold regions.

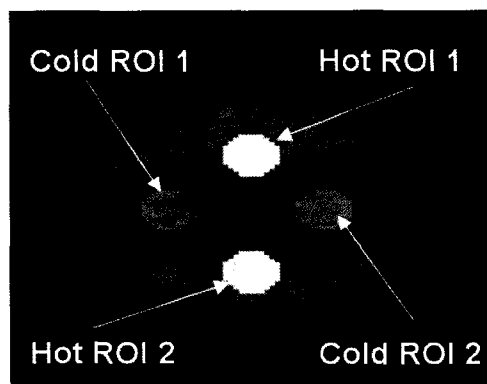


Figure 5.4. Regions of interest (ROI) drawn on the scatter correction phantom showing two cold ROIs and two hot ROIs. Each ROI was circular with a diameter of 5.5 mm.

The ratios of each cold ROI (CR1 and CR2) to each hot ROI (HR1 and HR2) were computed to obtain a total of 4 ratios for the scatter corrected and uncorrected images. It was assumed that the maximum activity recorded in the hot region served as

an accurate reference in the ratio computation. The average of these ratios was also computed to look at the overall scatter corrected ratio in comparison to non-corrected data. The data are summarized in Table 5.1.

Table 5.1. Comparison of the ratios for the cold and hot ROIs for uncorrected and scatter corrected data. Cold ROIs (CR) and hot ROIs (HR) as defined in Figure 5.4.

	CR1/HR1	CR1/HR2	CR2/HR1	CR2/HR2	Average
Uncorrected	0.116	0.115	0.145	0.145	0.130
Scatter Corrected	-0.016	-0.016	0.014	0.014	-0.004

From Table 5.1 it was observed that the scatter correction algorithm reduces the residual activity located inside the cold region cavity. The algorithm restored a near-zero activity in these regions as the average of ratios was closer to zero in comparison to the uncorrected data set. It was also noticed that the data corrected for scatter were overestimated in cold region 1 because a negative ratio was recorded, whereas, the correction was underestimated in region 2 because there still remained some uncorrected activity. Although these regions contained some variability, the overcorrection and under correction left less than 2% of the counts when compared to the active region. Figure 5.5 illustrates an image of the phantom before and after scatter correction. The figure includes a transverse slice centered axially in the cold rod region, along with coronal and sagittal views to see the effect of scatter correction on multiple axes.

In the case of Figure 5.5(a) there appeared to be residual activity recorded in the cold regions of the phantom and counts were also observed outside the phantom. With the scatter correction algorithm imposed, as illustrated in Figure 5.5(b), a reduction in the residual activity in the cold regions was observed, accompanied by the removal of some of the counts on the outside of the object. Moreover, the borders outlining the phantom

and the cold regions appeared more defined as a result of the scatter correction. These results confirmed visually that the removal of scatter counts enhance image quality by setting non-active regions to zero and by sharpening the edges.

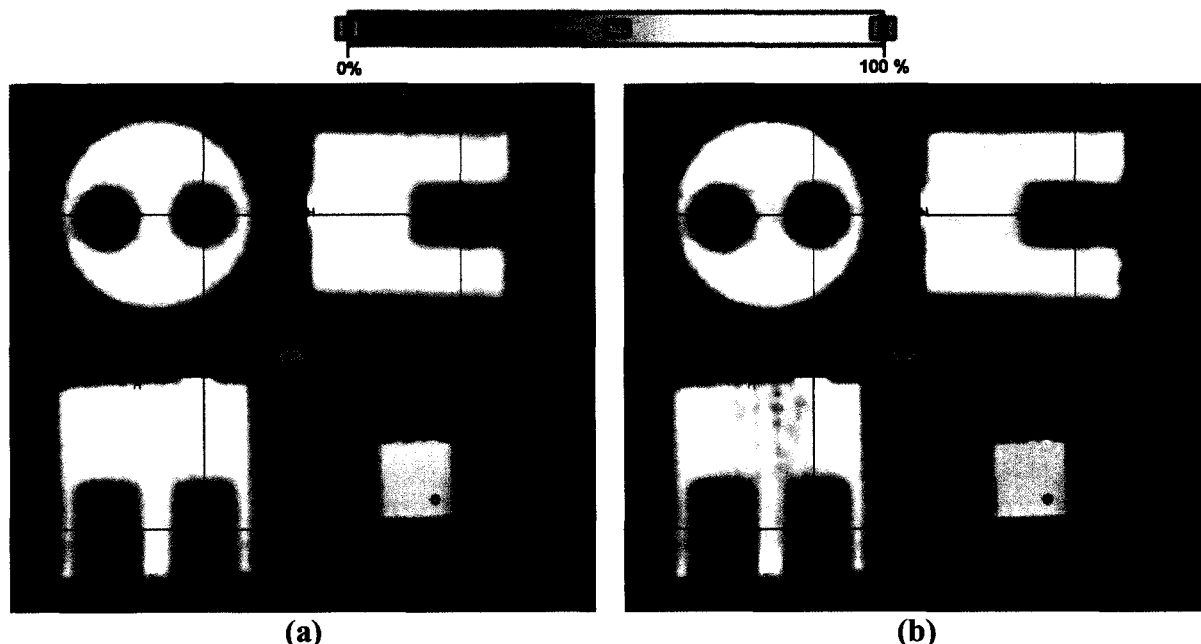


Figure 5.5. The cold rod phantom (a) before and (b) after scatter correction to demonstrate the removal of scattered counts in the cold region. The top left picture is a transverse image, the bottom left image is a coronal view and the top right is a sagittal view of the phantom with each slice defined by the crosshairs. The bottom right image shows the MIP.

After scatter correction, another phenomenon was encountered, as noticed in Figure 5.5(b), where there appears to be a loss of counts towards the middle of the object. As scatter was corrected, attenuation in the image was more visible. No transmission data were available for this study. Consequently, a calculated attenuation algorithm was explored for this case in order to restore the image quality. The attenuation correction algorithm that was used followed a similar approach to that found in [8]. However, the calculation was done solely in sinogram space prior to reconstruction. The first step was to detect the edges of the sinogram, which were already available from the scatter correction algorithm. The calculated attenuation algorithm that was used then deviated

from that found in [8] because attenuation lengths were assigned using a chord length calculation directly in sinogram space instead of reconstructing the image and assigning attenuation lengths in image space. The geometry of a circle was thus utilized to calculate the attenuation correction factors. This was permitted because the object in consideration was circular. For each pixel in the sinogram, which corresponds to an LOR, the length of the LOR that subtends the object was determined from the defined sinogram edges. This length is the chord length given by:

$$C = 2\sqrt{R^2 - d^2} \quad (5.2)$$

where C is the chord length, R is the radius of the circle and d is the distance from the chord to the origin. To aid in understanding this concept, Figure 5.6 shows the geometry employed in the algorithm. The chord length calculation effectively gives the total

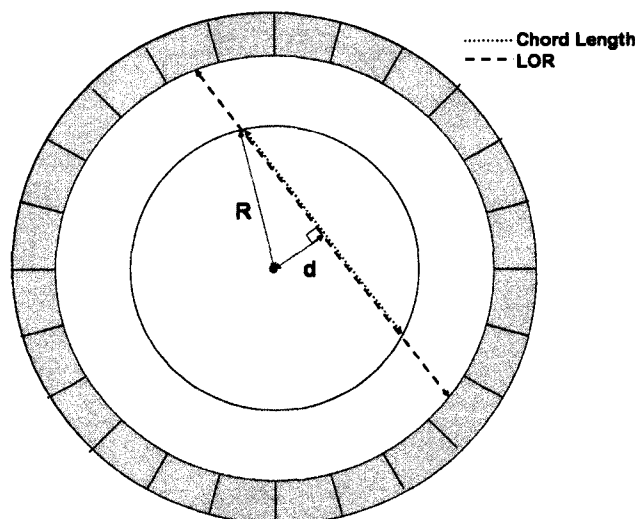


Figure 5.6. Chord length calculation through a circular object.

attenuation length through an object at a distance d from the origin at a given projection angle between two detectors (LOR).

After completion of the calculations the end result was sinograms where each pixel represents the attenuation length. These lengths may then be used to calculate the ACF sinograms. This was achieved for each pixel in the sinogram using the equation:

$$ACF = e^{\mu C} \quad (5.3)$$

This is equation 3.1 modified through replacement of the distance x with the chord length C . The factor μ takes the value 0.096 cm^{-1} for water at 511 keV. The narrow beam attenuation coefficient could be used because the scatter had been subtracted leaving only 511 keV photons detected. The ACF sinograms were then multiplied by the scatter corrected sinograms and then reconstructed using FBP. The resulting image is shown in Figure 5.7(b) with the original scatter corrected image shown in Figure 5.7(a).

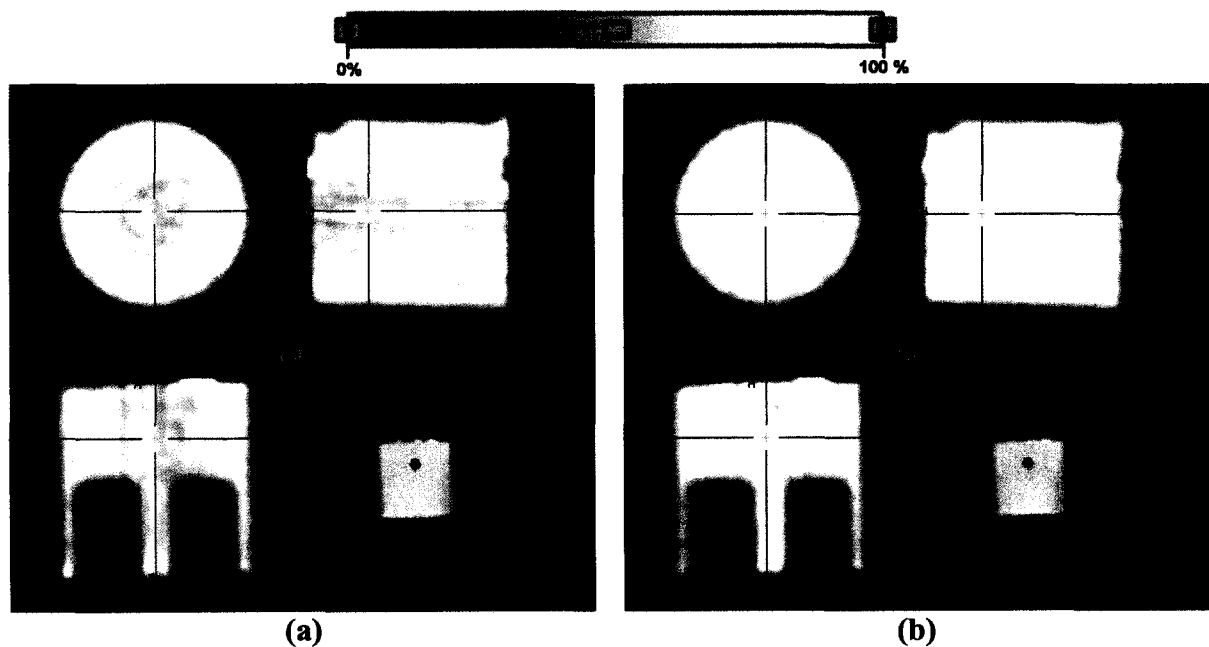


Figure 5.7. Calculated attenuation correction of the scatter corrected cold rod phantom data; (a) uncorrected (b) attenuation corrected. The crosshairs are repositioned over the uniformity region to better illustrate the effect of the attenuation correction. The coronal and sagittal planes are also shown along with the MIP.

The transverse image of the uniformity region in the phantom is shown along with the coronal and sagittal views to allow full visualization of the correction. To analyze the

data set, the uniform section of the phantom was considered by drawing a region of interest 22.5 mm in diameter within the central region of the transverse slice. The axial length of the region was 12 cm. The uniformity was then calculated by equation 4.17 for the images reconstructed with no correction, with scatter correction and with both scatter and attenuation correction. The results are shown in Table 5.2.

Table 5.2. Uniformity calculations to assess corrections in the cold rod phantom.

Image	Non-Uniformity (%)
No Correction	4.9
Scatter Corrected	9.1
Scatter and Attenuation Corrected	6.3

The measurements of uniformity show that the scatter correction algorithm caused image quality to deteriorate. This is because scatter correction will decrease the counts predominantly towards the center of an object leaving only photons that have undergone absorption governed by the attenuation coefficient μ . After a calculated attenuation correction algorithm was applied to the data, the uniformity was in part restored suggesting successful attenuation correction and restoration of image accuracy.

5.4. Discussion

The phenomena of photon attenuation and scatter have been shown to have a negative effect on image quality because of lost counts and mispositioned events. The correction for these phenomena has been shown to be feasible on the LabPET4™ scanner to aid in restoring the accuracy of the data. To decide on a practical method to be incorporated, many factors must be taken into consideration. These include the accuracy of the corrections, the practicality, and the overall effect on image quality.

Attenuation correction by transmission imaging was shown to have a positive effect on image quality by increasing the image uniformity and producing a flatter

response across a uniform object. When considering attenuation correction by transmission measurements, several factors must be considered. Firstly, a long transmission scan was needed to obtain usable data statistics for calculation of the ACFs. One of the problems with transmission imaging using an external positron emitter source, is that the source is located near the detector ring. The effect is that dead time will increase, thus lowering the total number of counts that may be recorded. This fact further supported the need for a dead time correction algorithm integrated in the scanner software. Additionally, the transmission scan time must be limited in small animals mainly because motion may occur between the transmission and emission acquisition. If the animal moved throughout the duration of the scan, the application of the ACFs derived from transmission data will be misaligned spatially, resulting in improper correction of the emission data because the attenuation coefficient distributions would not be properly matched. To limit the motion of the animals, anaesthetic is administered, however, this has to be done in moderation so that the animal will not die. Moreover, prolonged anaesthetic usage can have the same effect in killing the animal. Therefore, a two hour transmission scan is unreasonable. Although this method has been demonstrated to be effective in correcting for attenuation, to be fully implemented on a routine basis, increased data statistics would be needed so a realistic transmission scan of an animal could be obtained (approximately 10 minutes). A possible solution would be to use singles to measure transmission. Because this relies on source position to define an LOR, the detectors near the source are not counting, thus dead time will not limit the counting statistics, permitting for a much shorter scan time.

Another factor to regard in transmission imaging is that scatter was also recorded in the transmission data and was not corrected for in this study. To assess the magnitude of the scatter in the ACF measurements from transmission data, the calculated attenuation algorithm was employed for the uniformity phantom. A profile was then drawn across the central transverse sinogram of the ACFs for both of the measured and calculated profiles as shown in Figure 5.8. To check the validity of the ACFs, the broad beam attenuation coefficient, measured in chapter 3, was also applied in the calculated attenuation algorithm and a profile across the ACFs was also shown on the figure.

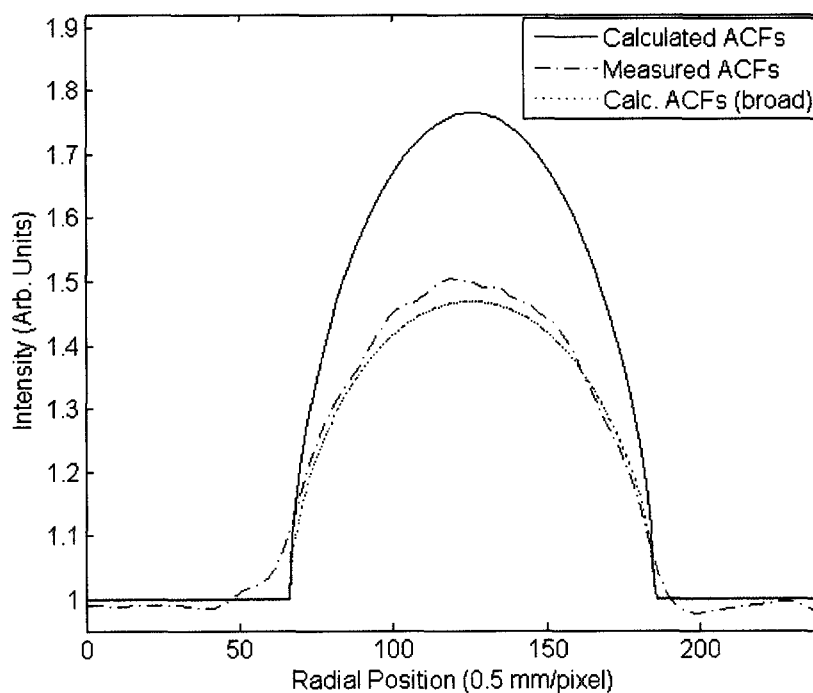


Figure 5.8. Profiles across the ACF sinograms from the narrow beam calculated attenuation (black) the transmission attenuation measurement (red) and the broad beam calculated attenuation (blue) for the uniform phantom.

It is clear from the figure that scattered events recorded in the transmission data have the effect of broadening and reducing the ACFs. The apparent shapes of the profiles are similar, which can be verified through replacement of the narrow beam attenuation

coefficient with the broad beam attenuation coefficient denoted by the blue line in the figure.

The emission data and the transmission data have different scatter distributions due to the activity distribution and source location. The broad beam calculated ACFs and measured ACFs profiles suggest that scatter in the emission data are partly corrected for. When the ratio of the blank to transmission data is taken, the scatter distribution accompanying the transmission data are also inverted. The shape of the scatter distribution for a uniform cylinder, as measured with the Gaussian fitting algorithm, shows there are more scatter events towards the center of the object. Thus, in a uniform circular object, the overall effect is that the ACFs measured by transmission will in part correct for scatter because the emission data have more scatter towards the center of the object while the ACFs are decreased because of scatter towards the center of the object. This can be confirmed by considering the profiles shown across the phantom before and after applying transmission ACFs in Figure 5.1. The flat response supports the notion that some of the scatter must have been corrected for suggesting that the underestimated ACFs have the effect of correcting scatter. If the scatter is not corrected, we would expect a scatter distribution added into the emission data. This operation is a multiplication process rather than a subtraction; therefore, a distribution of scattered counts in the attenuated corrected image is still observed on the outside of the object. To fully remove scatter in both the emission and transmission data, an alternative method needs to be considered. The difficulty in scatter correcting the measured ACFs is that the ratio of blank to transmission data has already been computed. Consequently, scatter correction needs to be done directly on the transmission data. The problem, however, is

that the data are not normalized and are noisy, making it very difficult to assign the correct edges in image space. A proposed solution would be to normalize the transmission data and use the calculated scatter correction algorithm to find the scatter distribution. This distribution would then be subtracted from the normalized transmission data and the scatter free ACFs would then be computed by taking the inverse of the corrected data. Following the same concept, the emission data would be separately corrected for scatter. The two could then be multiplied together to obtain scatter and attenuation free emission sinograms.

The calculated scatter correction algorithm was shown to reduce the scatter in the image, thus improving the accuracy of the data and the contrast in the image. The over- and under-estimates of the scatter contribution show that there is variability in the measurement, however, this was shown to be less than 2%. This variability can be attributed to the differences in the activity distribution in the cold rods when the emission data had not been corrected for scatter. These differences would then translate into the scatter correction algorithm. One of the limitations of the algorithm was that an assumption had been made that the scatter distribution was slowly varying. Although this assumption was valid for this case since the phantom had a relatively uniform attenuation coefficient distribution, when considering this algorithm for live animals it must account for large variations, such as air in the lung or abdomen. These regions have a significantly lower attenuation coefficient ($\mu = 1.04 \times 10^{-4} \text{ cm}^{-1}$ [43]), thus the scatter distribution would be different. This algorithm would have to be re-evaluated with the cold regions filled with air to study the differences of the scatter distributions.

For the present case, the scatter correction algorithm validity is supported by the subsequent calculated attenuation correction. The scatter events were corrected for, thus attenuation should be governed by the narrow beam attenuation coefficient. It is observed that after applying the calculated attenuation algorithm, assuming the narrow beam case, the non-uniformity and homogeneity are in part restored, thereby supporting the correct removal of scattered events. This comes at a cost, however, because the scatter contribution lying within the cold regions is increased after attenuation correction. The average ratio in the cold region to hot regions was found to be 3.4%, in contrast to the 0.4% recorded with only scatter correction. In comparison, the recorded ratio was 13% in the uncorrected image, therefore, scatter has been corrected for by a factor of 3.8. Some of the scattered events are therefore corrected and an overall increase in image quality was noted. This algorithm should be tested in cardiac imaging of rats and mice in the future to aid in the removal of scatter events. However, these cases are more challenging because a uniform activity distribution is not observed in the animals. Instead a largely variable activity distribution is recorded making it difficult to define a scatter background and an activity uptake region in the edge detection algorithm.

It was noticed after the calculated attenuation correction had been applied that the non-uniformity of 6.3% was not an improvement over the original value of 4.9% recorded without any corrections. Firstly, the calculated non-uniformity without any corrections may be subject to scatter and attenuation having compensatory effects as discussed previously. With the scatter correction imposed on the data, the non-uniformity of the image increased since there was now attenuation of photons towards the center of the image that increased the variability of the data. Furthermore, the attenuation

correction restored the uniformity because the lower counts towards the center of the object were corrected. The difference in non-uniformity between the uncorrected and the scatter and attenuation corrected image can thus be attributed to the compensation effect and noise introduced by the correction algorithms. The region of interest was drawn in the center of the object and does not analyze the data outside of the object. The scatter correction was shown to improve sharpness, therefore the non-uniformity measurement did not take this into consideration. The correction algorithms also introduced noise into the emission data. First, the edge detection algorithm may not exactly define the borders between the activity and scatter regions because of the discretized sinogram sampling. Furthermore, a constant attenuation coefficient was assumed, thus small variations were not taken into consideration when doing the scatter or attenuation correction even though the attenuation coefficient is higher in plastic. The constant scatter distribution assumed consequently introduced noise and this can be seen in the multiplication process, as the variability in the cold regions increases. These factors will introduce noise and offer an explanation as to why the uniformity is reduced in the final corrected image when compared to the uncorrected one.

The calculated attenuation algorithm could be used in this case because both cold cavities were filled with water. If the cavities had been filled with air, this calculation would not be accurate because a constant attenuation coefficient was assumed. A more robust approach would have to be utilized, especially in cardiac imaging where air is located inside the lungs. Furthermore, a circular geometry was assumed which is not the case in animals. The algorithm would have to be adjusted to accommodate for the true shape of the small animals. Although this works for the present case, a more flexible

method would have to be adopted in considering calculated attenuation correction for cardiac imaging. Transmission imaging is favourable because it makes no assumption of attenuation distribution or shape of the object, and the ACFs are determined directly for each individual LOR. As discussed, the transmission images also contain scatter. For images to be fully quantified, both the emission and transmission images must be corrected for scatter prior to calculating the ACFs multiplied by emission data. This is the next step in development to fully quantify cardiac imaging in rats and mice. Once the problems of poor data statistics are addressed in transmission imaging, the attenuation correction may be used after correcting for scatter in order to obtain suitable image accuracy and increased contrast in the absence of scatter and attenuation. This methodology is expected to be incorporated onto the LabPET4™ scanner directly in the near future.

The analysis presented in this chapter assessed scatter and attenuation correction using FBP because MLEM sinogram reconstruction was unavailable. It was observed that the profiles shown in Figure 5.1 have more noise than those across the phantom reconstructed with MLEM in Figure 4.17 even though they are the same experiment. It was therefore concluded that FBP has a higher tendency to amplify noise and that the statistical methods inherently have better image quality because the data statistical properties are taken into consideration in the reconstruction process. With the adoption of MLEM sinogram reconstruction, these algorithms may be further tested to be more comparable to animal studies as these are done with MLEM.

Attenuation and scatter correction have been shown to be feasible on the LabPET4™ scanner in phantom studies. The corrections have also been shown to partly

restore image quality and reduce the overall scatter background recorded. With improvements and new algorithms, transmission imaging with the presented scatter correction algorithm should be an effective way to correct for attenuation and scatter in small animals. This combination may be explored as a first step and implemented on the LabPET4™ scanner in the near future. Furthermore, other algorithms for the corrections should be explored to obtain improved quantification with this scanner. This analysis serves as a precursor to developing an optimal method for scatter and attenuation correction.

Chapter 6 - Conclusion

The LabPET4™ system has the capability for static FDG uptake imaging in small animals with its quasi individual crystal coupling to avalanche photodiode channels and its highly parallel digital electronics which allow for a sufficient count rate. A method for assessing the scanner's daily performance was developed and was shown to be an effective foundation for quality assurance. A performance evaluation of the camera has demonstrated its ability for static cardiac FDG imaging in rats and mice. The optimal activity to inject into a mouse and a rat to obtain the best signal to noise ratio in the reconstructed images was found to be 110 MBq and 156 MBq respectively. However, the peak NEC was found to be a factor of 20 lower than the expected value as quoted by the manufacturer. The sensitivity was also low in comparison to the quoted specification. The peak NEC and sensitivity measurements suggest that improvements on the scanner should be made to address these issues. In contrast, the camera demonstrates the necessary resolution and count rate for imaging FDG uptake in the left ventricle in rats and mice with the optimal resolution being recorded at 1.2 mm. The normalization available on the LabPET4™ provides a suitable detector efficiency correction with a non-uniformity of 9.2% recorded over the entire axial field of view.

Dead time limits the quantification available on a PET scanner and these effects were shown to be significant at the peak NEC suggesting that a dead time correction algorithm should be imposed on the LabPET4™ scanner. An assessment of the magnitude of attenuation and scatter has shown that these effects are non-negligible and corrections for these phenomena should be considered for rat and mouse sized objects. It was found when imaging mouse-like and rat-like geometries that 22% and 28% of the

random corrected counts are in the form of scatter. An initial evaluation on attenuation and scatter correction in phantoms demonstrates that these corrections are possible on the scanner. Furthermore, the corrections have positive effects on overall image quality through increasing the contrast and the accuracy of the corrected images.

The performance evaluation and corrections done throughout this work have suggested new studies that could be performed in the future. A re-evaluation of the sensitivity could be done using a line source measurement in order to obtain a sensitivity profile across the axial FOV. This would aid in understanding how sensitivity changes with source position. Furthermore, the scatter fraction measurements were compared to those of other systems, and the results suggest that the end shield inserts should be studied to evaluate their effect on the scatter fraction and the NEC curves. A dead time correction model should also be introduced in order to create a wider range of activity for quantitative imaging. Finally, the attenuation and scatter correction algorithms were only performed on phantom studies. These studies should be translated into live animals to study the accuracy of these corrections. In conclusion, more sophisticated correction algorithms may be needed to improve the image quantification in vivo.

Appendix A – Cardiac Rat Phantom

In order to perform and validate scatter and attenuation correction for rats, a thoracic phantom was designed that incorporated a rat's geometry while maintaining simplicity and robustness. The phantom was constructed from plastic with an attenuation coefficient similar to soft tissue. Geometrical data acquired from a rat dissection were combined with data found in literature to create the phantom. Figure A.1 shows the exposed thoracic cavity of a 285 g rat where the rib cage has been removed. The intention was to create a phantom that represents the left ventricle (LV) when imaged using PET while introducing other important organs such as the liver and lungs. The design, therefore, includes the LV, lungs, and liver, which are believed to be the most representative organs for cardiac imaging of a live rat. The LV is the primary muscle of the heart responsible for circulating blood into the body. Glucose may be used as a major source of energy of the heart and glucose analogs, such as ^{18}F -FDG, tend to accumulate here. The liver is another place where radiotracers are likely to gather and because of its location approximately 1 cm below the heart, activity from this region will contaminate heart images in the form of scatter. The lungs were incorporated because they also affect images due a lower attenuation coefficient in comparison to muscle tissue. The purpose was to design a phantom that integrates these portions of the rat anatomy so that the phantom can be used to simulate a scan with a live rat. This design represents an approximation to the true rat geometry. Average measurements were computed for the LV and lungs in order to approximate the living rat into a static model. Additionally, all components were approximated to be cylindrical for design simplicity. The final phantom design is displayed in Figure A.2.

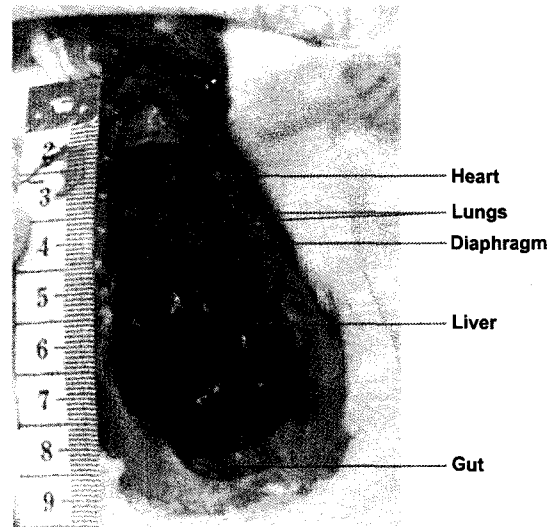


Figure A.1. Exposed thoracic cavity of a 285 g rat.

Prior to dissection, the thoracic cavity of the rat was measured to have a circumference of 17 cm, resulting in the phantom having an outer radius of 2.7 cm with the cylindrical approximation. The cavity was then opened and the rib cage was removed. Primarily the lung cavity was considered. The length of the lungs was determined to be 2 cm, as can be verified from Figure A.1. Next, the lung volume was estimated from [35] where a rat was imaged using CT. The expiration and inspiration volumes were measured to be 10.1 mL and 21.3 mL respectively. Assuming that 67% of the time the lungs are in expiration and 33% of the time in inspiration, a weighted average was computed to give an average volume of 13.8 mL. The radius of the lung cavity was thus calculated to be 1.5 cm using the cylindrical geometry. The cavity was positioned 6 mm from the surface of the phantom, which was estimated from a measurement of the outside skin to lung. Both lungs are considered to be one solid cylinder. Also, an injection port was introduced to allow for water or a radiotracer to be placed in the cavity. Figures A.2(a), A.2(b) and A.2(d) show the location of the lungs inside the phantom.

Next, the geometry of the LV was examined. Values for the LV's end diastolic volume (EDV) and end systolic volume (ESV) for a healthy adult rat can be found in [36-38]. An average value was calculated from a total of five EDVs and ESVs. A weighted average was then taken with the assumption that the heart spends 67% of the time in the diastolic phase and 33% of the time in the systolic phase. The average volume found was 325 μL . The length of the LV was measured to be 1 cm and the myocardium thickness (muscle tissue around LV) was estimated to be 3 mm. Utilizing the volume and length measurements, the radius of the LV was calculated to be 0.3 cm. The myocardium is where many radiotracers of interest accumulate; therefore, the chamber was hollowed out to allow for injection, while the inner part was plastic. The myocardium thickness was obtained by averaging actual measurements of the myocardium at the apex and top of the LV. Finally, the wall thickness of the LV in the rat was measured to be 2 mm; however, in the phantom this quantity was adjusted to 3 mm to ensure design stability.

Furthermore, the LV cavity is situated at the top of the lung cavity to ensure that it could be manufactured. Also in the transaxial view of the phantom, the heart is situated in the lung cavity 6 mm from the edge and centered for symmetry purposes, as observed in Figures A.2(a), A.2(b) and A.2(d).

In PET imaging, the liver is responsible for a large scatter contribution, providing motivation for its introduction in the phantom design. The liver itself has a rather abnormal shape but has been adopted to be cylindrical inside the phantom for simplicity. The length of the liver was found to be ~ 3 cm, and the diameter of the cylinder was estimated to be 1.5 cm. The distance between the bottom of the lung cavity and the liver was set to be 3 mm, again to ensure durability of the design. A hole is also positioned to

allow for injection into liver cavity. The liver location can be examined in Figures A.2(c) and A.2(d).

The length of the phantom was arbitrarily defined to be 10.3 cm so that an additional 3 cm was added to the top (above the LV/Lung) and an additional 2 cm to the bottom (below the liver) in order to simulate the scatter contribution from outside of the thoracic cavity.

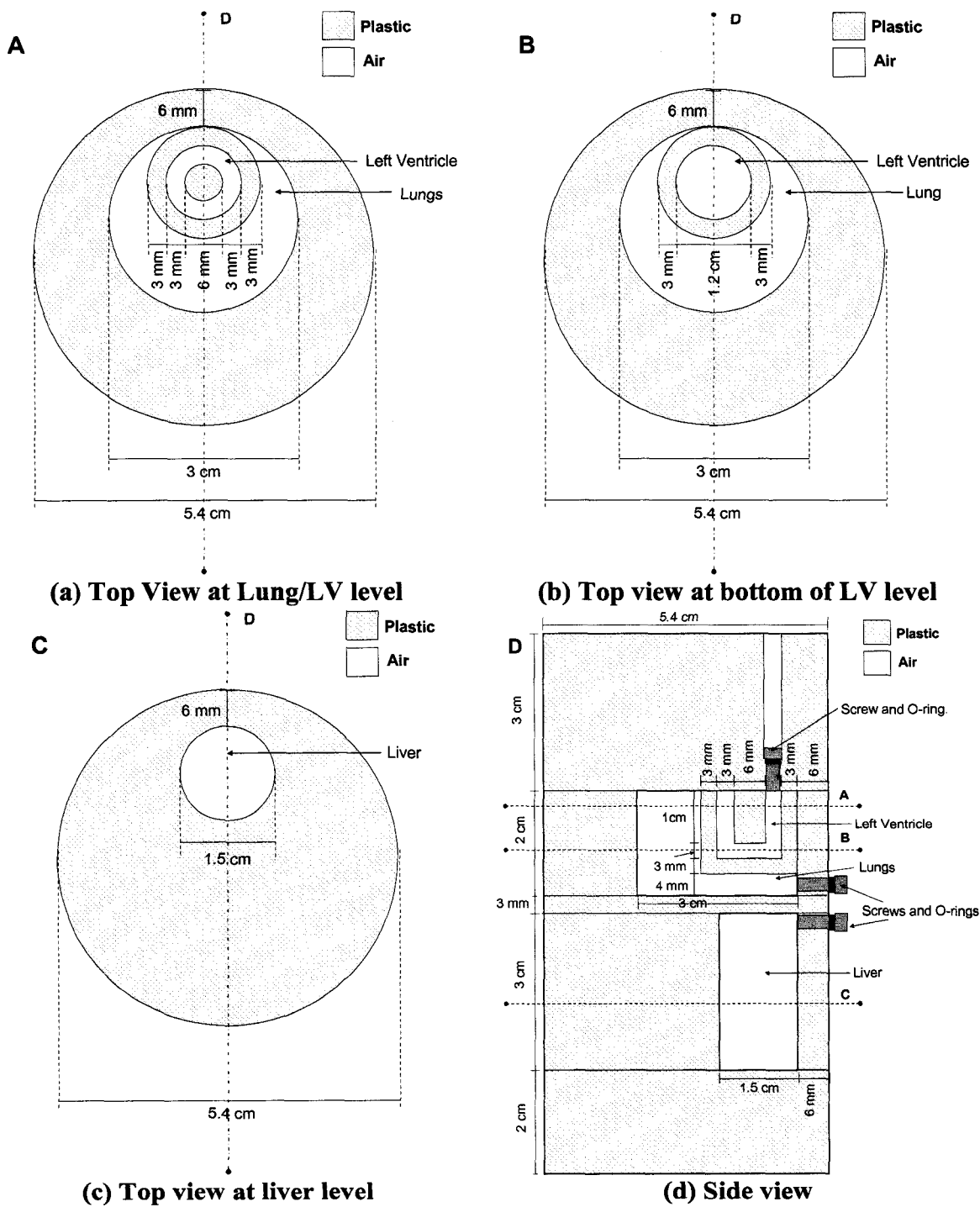


Figure A.2. The cardiac rat phantom shown schematically.

References

- [1] Dumouchel,T., Selivanov,V., Cadorette,J., Lecomte,R., Dekemp,R.A., MLEM Reconstructed Image Resolution from the LabPET Animal Scanner, Conf. Rec. 2006 IEEE NSS/MIC, (2006).
- [2] Dumouchel,T., Bergeron,M., Cadorette,J., Lepage,M., Selivanov,V., Lapointe,D., DaSilva,J., Lecomte,R., Dekemp,R.A., Initial Performance Assessment of the LabPET™ APD-Based Digital PET Scanner, J. Nucl. Med., 48 (2007) 132P (Abstract).
- [3] Rosenthal,N., Brown,S., The Mouse Ascending: Perspectives for Human-Disease Models, Nat. Cell Bio., 9 (2007) 993-999.
- [4] Bacharach,S.L., In Bergmann,SR, Sobel,BE (Eds.), Positron Emission Tomography of the Heart Futura Publishing Company Inc., Mount Kisco, NY, 1992, pp. 13-44.
- [5] Cherry,S.R., Dahlbom,M., PET: Physics, Instrumentation, and Scanners. In Phelps,ME (Ed.), PET: Molecular Imaging and Its Biological Applications Springer-Verlag New York, Inc., New York, NY, 2004, pp. 1-124.
- [6] Knoll,G.F., Radiation Detection and Measurement, John Wiley & Sons, New York, 1989.
- [7] Bergstrom,M., Litton,J., Eriksson,L., Bohm,C., Blomqvist,G., Determination of Object Countour from Projections for Attenuation Correction in Cranial Poistron Emission Tomography, J. Comp. Assist. Tomogr., 6 (1982) 365-372.
- [8] Siegel,S., Dahlbom,M., Implementation and Evaluation of a Calculated Attenuation Correction for PET, IEEE Trans. Nucl. Sci., 39 (1992) 1117-1121.

- [9] Meikle,S.R., Dahlbom,M., Cherry,S.R., Attenuation Correction Using Count-Limited Transmission Data in Positron Emission Tomography, *J. Nucl. Med.*, 34 (1992) 143-150.
- [10] Dekemp,R.A., Nahmais,C., Attenuation Correction in PET using Single Photon Transmission Measurement, *Med. Phys.*, 21 (1994) 771-7778.
- [11] Yu,S.K., Nahmais,C., Single-Photon Transmission Measurement in Positron Tomography using ^{137}CS , *Phys. Med. Bio.*, 40 (1995) 1255-1266.
- [12] Karp,J.S., Muehllehnew,G., Qu,H., Yan,X.-H., Singles Transmission in Volume-imaging PET with a ^{137}CS Source, *Phys. Med. Bio.*, 40 (1995) 929-944.
- [13] Stearns,C.W., Scatter Correction Method for 3D PET using 2D Fitted Gaussian Functions, *J. Nucl. Med.*, 36 (1995) 105P (Abstract).
- [14] Cherry,S.R., Huang,S.-C., Effects of Scatter on Model Parameter Estimates in 3D PET Studies of the Human Brain, *IEEE Trans. Nucl. Sci.*, 42 (1995) 1174-1179.
- [15] Bergstrom,M., Eriksson,L., Bohm,C., Blomqvist,G., Litton,J., Correction for Scattered Radiation in a Ring Detector Positron Camera by Integral Transformation of the Projections, *J. Comp. Assist. Tomogr.*, 7 (1983) 42-50.
- [16] Grootoenk,S., Spinks,T.J., Sashin,D., Spyrou,N.M., Jones,T., Correction for scatter in 3D brain PET using a dual energy window method, *Phys. Med. Biol.*, 41 (1996) 2757-2774.
- [17] Watson,C.C., Newport,D., Casey,M.E., Dekemp,R.A., Beanlands,R.S., Schmand,M., Evaluation of simulation-based scatter correction for 3-D PET cardiac imaging, *IEEE Trans. Nucl. Sci.*, 44 (1997) 90-97.
- [18] Ollinger,J.M., Model-Based Scatter Correction for Fully 3D PET, *Phys. Med. Biol.*, 41 (1996) 153-176.

- [19] Levin,C.S., Dahlbom,M., Hoffman,E.J., A Monte Carlo Correction for the Effect of Compton Scattering in 3-D PET Brain Imaging, *IEEE Trans. Nucl. Sci.*, 42 (1995) 1181-1185.
- [20] Bailey,D., Meikle,S., A Convolution-Subtraction Scatter Correction Method for 3D PET, *Phys. Med. Biol.*, 39 (1994) 411-424.
- [21] Popescu,L.M., Lewitt,R.M., Matej,S., Karp,J.S., PET Energy-Based Scatter Estimation and Image Reconstruction with Energy-Dependent Corrections, *Phys. Med. Biol.*, 51 (2006) 2919-2937.
- [22] Bentourkia,M., Msaki,M., Cadorette,J., Lecomte,R., Object and Detector Scatter-Function Dependence on Energy and Position in High Resolution PET, *IEEE Trans. Nucl. Sci.*, 42 (1995) 1167.
- [23] Chuang,K.-S., Wu,J., Jan,M.-L., Chen,S., Hsu,C.-H., Novel Scatter Correction for Three-Dimensional Positron Emission Tomography by use of a Beam Stopper Device, *Nucl. Inst. Meth. Phys. Res. A*, 441 (2005) 540-552.
- [24] Defrise,M., Kinahan,P.E., Data Acquisition and Image Reconstruction for 3D PET. In Bendriem,B, Townsend,DW (Eds.), *The Theory and Practice of 3D PET* Kluwer Academic Publishers, Netherlands, 1998, pp. 10-53.
- [25] Prince,J.L., Jonathan,M.L., *Medical Imaging Signals and Systems*, Pearson Education, Inc., Upper Saddle River, NJ, 2006.
- [26] Humm,J.L., Rosenfeld,A., Del Guerra,A., From PET Detectors to PET Scanners, *Eur. J. Nucl. Med. Mol. Imaging*, 30 (2003) 1574-1597.
- [27] Lecomte,R., Dekemp,R.A., Dumouchel,T., Thorn,S., Cadorette,J., Lapointe,D., Lepage,M.D., Pinet,M., Robert,G., Selivanov,V., Bélanger,F., Lemieux,F., Semmaoui,H., Tétrault,M.-A., Viscogliosi,N., Bergeron,M., Fontaine,R., Initial Results with LabPET™, a Second-Generation APD-Based Digital PET Scanner for High-Performance Pre-Clinical Molecular Imaging, *Conf. Rec. 2006 IEEE NSS/MIC*, (2006).

- [28] Fontaine,R., Bélanger,F., Viscogliosi,N., Semmaoui,H., Tétrault,M.-A., Michaud,J.-B., Pepin,C., Cadorette,J., Lecomte,R., The Architecture of LabPET™, a Small Animal APD-Based Digital PET Scanner, Conf. Rec. 2005 IEEE NSS/MIC, (2005) 2785-2789.
- [29] Selivanov,V.V., Picard,Y., Cadorette,J., Rodrigue,S., Lecomte,R., Detector Response Models for Statistical Iterative Image Reconstruction in High Resolution PET, IEEE Trans. Nucl. Sci., 47 (2000) 1168-1175.
- [30] Animal PET Scanner Task Force, Animal PET Scanner Standard (Under Revision), Submitted to the National Electrical Manufacturers Association, (2006).
- [31] Strother,S.C., Casey,M.E., Hoffman,E.J., Measuring PET Scanner Sensitivity: Relating Countrates to Image Signal-to-Noise Ratio using Noise Equivalent Counts, IEEE Trans. Nucl. Sci., 37 (1990) 783-788.
- [32] NEMA Standards Publication NU2-2001: Performance Measurement of Positron Emission Tomographs, National Electrical Manufacturers Association, Rosslyn, VA, 2001.
- [33] Eriksson,L., Watson,C.C., Wienhard,K., Eriksson,M., Casey,M.E., Knoess,C., Lenox,M., Burbar,Z., Conti,M., Bendriem,B., Heiss,W.D., Nutt,R., The ECAT HRRT: An Example of NEMA Scatter Estimation Issues for LSO-Based PET Systems, IEEE Trans. Nucl. Sci., 52 (2005) 90-94.
- [34] Watson,C.C., Casey,M.E., Eriksson,L., Mulnix,T., Adams,D., Bendriem,B., NEMA NU 2 Performance Tests for Scanners with Intrinsic Radioactivity, J. Nucl. Med., 45 (2004) 822-826.
- [35] Cao,M., Stantz,K.M., Liang,Y., Krishnamurthi,G., Presson,R.G.Jr., Assessment of Multislice CT to Quantify Pulmonary Emphysema Function and Physiology in a Rat Model, Proceedings of the SPIE - The International Society for Optical Engineering, 5764 (2005) 498-506.

- [36] Croteau,E., Benard,F., Cadorette,J., Gauthier,M.E., Aliaga,A., Bentourkia,M., Lecomte,R., Quantitative Gated PET for the Assessment of Left Ventricular Function in Small Animals, *J. Nucl. Med.*, 44 (2003) 1655-1661.
- [37] Al Shafei,A.I., Wise,R.G., Gresham,G.A., Carpenter,T.A., Hall,L.D., Huang,C.L., Magnetic Resonance Imaging Analysis of Cardiac Cycle Events in Diabetic Rats: The Effect of Angiotensin-Converting Enzyme Inhibition, *J. Physiol*, 538 (2002) 555-572.
- [38] Maskali,F., Franken,P.R., Poussier,S., Tran,N., Vanhove,C., Boutley,H., Le Gall,H., Karcher,G., Zannad,F., Lacolley,P., Marie,P.Y., Initial Infarct Size Predicts Subsequent Cardiac Remodelling in the Rat Infarct Model: an In Vivo Serial Pinhole Gated SPECT Study, *J. Nucl. Med.*, 47 (2006) 337-344.
- [39] Laforest,R., Longford,D., Siegel,S., Newport,D.F., Yap,J., Performance Evaluation of the microPET - Focus-F120, *IEEE Trans. Nucl. Sci.*, 54 (2007) 42-49.
- [40] Missimer,J., Madi,Z., Honer,M., Keller,C., Chubiger,A., Ametamey,S.-M., Performance Evaluation of the 16-Module quad-HIDAC Small Animal PET Camera, *Phys. Med. Bio.*, 49 (2004) 2069-2081.
- [41] Bergeron,M., Cadorette,J., Lepage,M.D., Robert,M., Selivanov,V., Tétrault,M.-A., Viscogliosi,N., Fontaine,R., Dumouchel,T., Thorn,S., DaSilva,J., Dekemp,R., Lecomte,R., Performance Evaluation of the LabPET™ APD-Based Digital PET Scanner, 2007 IEEE NSS/MIC (Abstract Accepted), (2007).
- [42] Watson,C.C., Townsend,D.W., Bendriem,B., PET/CT Systems. In Wernick,MN, Aarsvold,JN (Eds.), *Emission Tomography Elsevier Inc.*, San Diego, CA, 2004, pp. 195-212.
- [43] Hubbell,J.H., Seltzer,S.M., *Tables of X-Ray Mass Attenuation Coefficients and Mass Energy-Absorption Coefficients 1 keV to 20 MeV for Elements Z = 1 to 92 and 48 Additional Substances of Dosimetric Interest*, U.S. Department of

Commerce, Technology Administration National Institute of Standards and
Technology, Gaithersburg, MD, 1995.